# Angular momentum transport modeling: achievements of a gyrokinetic quasi-linear approach

P. Cottier, C. Bourdelle, Y. Camenen, O.D. Gurcan, F.J. Casson, Xavier Garbet, P. Hennequin, T. Tala

**HAL Id: hal-00926719**

**https://hal.archives-ouvertes.fr/hal-00926719**

Submitted on 10 Jan 2014

# Angular momentum transport modeling: achievements of a gyrokinetic quasi-linear approach

**P Cottier[1], C Bourdelle[1], Y Camenen[2], Ö D Gürcan[3], F J Casson[4], X Garbet[1], P Hennequin[2] and T Tala[5]**

IRFM, CEA, F-13108 Saint Paul-Lez-Durance, France

E-mail: `pierre.cottier@cea.fr`
PIIM UMR 7345, CNRS, Aix-Marseille Univ., Marseille, France
LPP UMR 7648, CNRS-Ecole Polytechnique, Palaiseau, France
Max-Planck-Institut für Plasmaphysik, IPP-Euratom Association,
Garching-bei-München, Germany
VTT, Association Euratom-Tekes, PO Box 1000, FIN-02044 VTT, Finland

**Abstract.** QuaLiKiz, a model based on a local gyrokinetic eigenvalue solver[1] is expanded to include momentum flux modeling in addition to heat and particle fluxes[2, 3]. Essential for accurate momentum flux predictions, the parallel asymmetrization of the eigenfunctions is successfully recovered by an analytical fluid model. This is tested against self-consistent gyro-kinetic calculations and allows for a correct prediction of the $\mathbf{E} \times \mathbf{B}$ shear impact on the saturated potential amplitude by means of a mixing length rule. Hence, the effect of the $\mathbf{E} \times \mathbf{B}$ shear is recovered on all the transport channels including the induced residual stress. Including these additions, QuaLiKiz remains $\sim 10000$ faster than non-linear gyro-kinetic codes allowing for comparisons with experiments without resorting to High Performance Computing. The example is given of momentum pinch calculations in NBI modulation experiments[4] for which the inward convection of the momentum is correctly predicted.

## 1. Introduction

Sheared flows in tokamaks have long been studied since there are both theoretical and experimental evidences that they can significantly enhance the plasma energy confinement [5–9]. The toroidal torque can result from the interaction of the turbulent plasma with the walls and the coils [10–12] or from the heating system such as NBI [13–15] or even RF heating[16]. The back-reaction of sheared flows on turbulence has received considerable attention, either its stabilizing effect with sheared *poloidal* rotation (related to sheared radial electric field via the $\mathbf{E} \times \mathbf{B}$ drift) [5, 8] or its destabilizing effect with parallel velocity gradient $\nabla u_\parallel$[17–19]. The interplay between mean flows and turbulence can be described quantitatively by quasilinear fluid models[20–22], non-linear gyro-fluid models[23, 24], quasilinear gyrokinetic models[4, 25, 26], and non-linear gyrokinetic simulations[27–33].

This paper presents a reduced model compatible with integrated modeling able to predict both momentum transport and sheared flows effects on turbulence for tokamak plasmas. This model is extending the QuaLiKiz transport code abilities which was developed to compute heat and particle fluxes [2]. The philosophy of QuaLiKiz is to minimize the number of *ad hoc* parameters. Only the saturated potential amplitude is prescribed once and for all to match the ion heat flux of non-linear gyrokinetic simulations for the GA-std case. Predicting quantitatively the turbulent fluxes without resorting to parameter fitting requires the use of a gyrokinetic linear solver. However two orders of magnitude in CPU time have to be gained to be compatible with the integrated modeling framework. Therefore, QuaLiKiz uses both the ballooning representation at lowest order, reducing the dimension of the problem to 3 from $(\mu,v_\parallel,r,\theta)$ to $(\mu,v_\parallel,r)$ by a Fourier decomposition in the radial direction, and trial eigenfunctions from the analytic fluid limit [1, 34]. QuaLiKiz is coupled to CRONOS, an integrated modeling platform that evolves consistently $q$, $T_e$, $T_i$ and $n_e$ profiles[35]. It has been used for the prediction of the heat transport in JET [36].

In the new version of QuaLiKiz, the impact of the plasma rotation on the eigenfunction is reproduced with satisfactory accuracy compared to self-consistent gyrokinetic codes through a complex shift of Gaussian eigenfunctions. The effect of this shift is included in the non-linear saturation rule through the use of an effective $k_\perp$ as detailed in Sec. 5. However different from the model proposed in [22], the method detailed in this work enables the recovery of the heat and particle flux stabilization with $\mathbf{E} \times \mathbf{B}$ shear. The induced residual stress can also be estimated with the benefit to be fitting-parameter free. However, the local approach taken in QuaLiKiz does not allow for a consistent treatment of higher $\rho^*$ effects characterizing the residual stress [37–39]. The heat and particle flux reduction with $\mathbf{E} \times \mathbf{B}$ shear match non-linear gyrokinetic simulations. The momentum flux sensitivity to $u_\parallel$ and $\nabla u_\parallel$ is also in agreement with non-linear gyrokinetic results and shows the importance to have the correct shape of the eigenfunctions in the parallel direction. Finally, the comparison with NBI modulation experiments showing the existence of an inward convective momentum flux in JET[4] is

successful. It underlines that separating the different contributions to the momentum flux is challenging. The fluxes sensitivity to the gradient estimations is highlighted, advocating for flux forcing of the code, which is to be done by coupling this new version to CRONOS integrated platform.

First, the linear eigenfunction/eigenvalue equation at the heart of the linear solver of QuaLiKiz is re-derived in Sec. 2 to include new terms coming from the plasma bulk rotation. Then, in Sec. 3, the fluid model calculating the eigenfunctions is revisited to include the sheared flow effects and compared to self-consistent gyrokinetic eigenfunctions from the gyrokinetic code GKW[40]. In Sec.4, the sensitivity to $u_{\parallel}$, $\nabla u_{\parallel}$ and $\mathbf{E} \times \mathbf{B}$ shear of QuaLiKiz linear growth rates are successfully benchmarked against GKW. In Sec. 5, the quasi-linear momentum flux is derived, the shape of the saturated potential is discussed and the estimations of heat, particle and momentum fluxes are compared to non-linear gyrokinetic simulations from GKW and GYRO. The methods to separate the different contributions to the momentum flux are discussed as well. Finally, in Sec. 6, a JET shot with NBI modulation [41] is modeled. The diffusive and convective terms are compared to the experimental values.

## 2. Linearized gyrokinetic dispersion relation

First, the linearized gyrokinetic equation is derived including the effect of a finite rotation of the plasma. The formalism employed in previous derivations without bulk rotation [1] is conserved and its validity range is discussed. Finally, the expression used for the linear solver in QuaLiKiz and based on the linearized Vlasov equation coupled with the electroneutrality condition is given.

To study the impact of the plasma rotation, the model has to allow for a finite equilibrium rotation of the system $u_{\parallel}$. In the gyrokinetic framework, this translates into having a finite value for $u_{\parallel} = \int f_0 v_{\parallel} \mathrm{d}^3 v$, the integral of the product of $f_0$, the equilibrium distribution function multiplied by the velocity coordinate $v_{\parallel}$. $f_0$ being chosen Maxwellian, it reads, for each species $s$ of density $n_s$, mass $m_s$, temperature $T_s$ and thermal velocity $v_{Ts} = \sqrt{2T_s/m_s}$:

$$f_0^s = \frac{n_s}{(2\pi T_s/m_s)^{3/2}} \exp\left(-\frac{E}{T_s} + \frac{u_{\parallel}(2v_{\parallel} - u_{\parallel})}{v_{Ts}^2}\right) \tag{1}$$

$v_{\parallel}$ being the parallel velocity coordinate, $E$ the energy defined by $E/T_s = v_{\parallel}^2/v_{Ts}^2 + \mu B/T_s$ and $\mu$ the adiabatic invariant. The reference frame being the laboratory frame here $\frac{u_{\parallel}}{v_{Ts}}$ is the Mach number for the species $s$. In core plasma of conventional tokamaks, the Mach number is usually limited to values smaller than 0.4. In spherical tokamaks, however, core Mach numbers can reach values close to unity[31]. The low Mach number limit is taken in the following and $f_0$ is developed up to second order in $\frac{u_{\parallel}}{v_{Ts}}$. Now, taking the linearized Vlasov equation in the angle-action variables $(\boldsymbol{\alpha}, \mathbf{J})$ and applying

quasi-neutrality in its variational form[42], one finds[1]:

$$\sum_s \left\langle \frac{\mathbf{n} \cdot \partial_{\mathbf{J}} f_0^s}{\omega - \mathbf{n} \cdot \partial_{\mathbf{J}} h_0 + \imath o^+} |\tilde{h}_{\mathbf{n},\omega}|^2 \right\rangle_{\mathbf{J},\boldsymbol{\alpha}} = 0 \tag{2}$$

where $\mathbf{J}$ are the actions i.e. the three invariants: $\mu$, $E$ and $p_\phi$ the angular momentum. $\boldsymbol{\alpha}$ are the associated angles defined by $\dot{\boldsymbol{\alpha}} = \partial_{\mathbf{J}} h_0$. $\mathbf{n}$ are the wave numbers associated with the angle variables $\boldsymbol{\alpha}$ through the Fourier decomposition of the fluctuating distribution function and fluctuating Hamiltonian[42]. $h_0$ is the unperturbed Hamiltonian defined by $h_0 = mv^2/2 + e\phi$. QuaLiKiz is an electrostatic code, the unperturbed Hamiltonian being reduced to its electrostatic part. The brackets $\langle \cdots \rangle_{\mathbf{J},\boldsymbol{\alpha}}$ mean integration over $\mathbf{J}$ and $\boldsymbol{\alpha}$. See Appendices A.1 and A.2 of [1] for a detailed derivation of the linearized Vlasov equation, its decomposition over the angle-action variables and how the electroneutrality condition is used to find (2). In the electrostatic limit, the perturbed Hamiltonian $\tilde{h}_{n\omega}$ is reduced to $e_s \tilde{\phi}_{n\omega}$. It is clear from this equation that terms proportional to the parallel velocity and its gradient, coming from $\mathbf{n} \cdot \partial_{\mathbf{J}} f_0$, will impact the linear response. To illustrate this, the diamagnetic frequency $\mathbf{n} \cdot \boldsymbol{\Omega}^* = \mathbf{n} \cdot \partial_{\mathbf{J}} f_0 - \mathbf{n} \cdot \partial_{\mathbf{J}} E/T_s$ is expressed as a function of the gradients $\nabla n_s$, $\nabla T_s$ and $\nabla u_\parallel$ in (3).

$$\mathbf{n} \cdot \boldsymbol{\Omega}_s^* = \frac{k_\theta T_s}{e_s B} \left[ \frac{1}{n_s} \frac{\mathrm{d}n_s}{\mathrm{d}r} + \left( \frac{E}{T_s} - \frac{3}{2} - \frac{u_\parallel}{v_{Ts}} \frac{2v_\parallel - u_\parallel}{v_{Ts}} \right) \frac{1}{T_s} \frac{\mathrm{d}T_s}{\mathrm{d}r} + 2 \left( \frac{v_\parallel - u_\parallel}{v_{Ts}} \right) \frac{1}{v_{Ts}} \frac{\mathrm{d}u_\parallel}{\mathrm{d}r} \right] \tag{3}$$

where $k_\theta = \frac{-nq}{r}$ is the poloidal wave vector in the ballooning representation presented later on, $n$ being the toroidal wave number, $q$ the safety factor and $r$ the radial coordinate. $e_s$ is the charge of the species $s$.

From (2), $\mathbf{n}\partial_{\mathbf{J}} h_0$ corresponds to the three frequencies associated with the three angle variables ($\mathbf{n}\partial_{\mathbf{J}} h_0 = \partial_t \boldsymbol{\alpha}$) characterizing the particles movement within the magnetic field of a tokamak, namely the cyclotron frequency, the parallel motion frequency (bounce frequency for trapped particles) and the – curvature, $\nabla B$ and $\mathbf{E} \times \mathbf{B}$ – drift frequency. Since the cyclotron frequency $\omega_c$ is much larger than the other characteristic frequencies, a scale separation is possible. The dependence over the gyro-angle can be removed either by averaging over the gyromotion according to historical gyrokinetic theory [43–46] or via Lie transforms according to modern gyrokinetics[47–50]. In the end, both methods result in multiplying the perturbed potential $\tilde{h}$ by the zero order Bessel function $J_0^2(k_\perp \rho_s)$ ; $\rho_s$ being the Larmor radius for the species $s$. Then $\mathbf{n} \cdot \partial_{\mathbf{J}} h_0 = \mathbf{n} \cdot \boldsymbol{\Omega}_{\mathbf{J}}$ corresponds to the gyrocenter drifts. In the simplified $\hat{s}-\alpha$ equilibrium, which QuaLiKiz is using, $\mathbf{n} \cdot \boldsymbol{\Omega}_{\mathbf{J}}$ can be written as expressed in (4). Using such an equilibrium leads to the underestimation of ITG linear growth rates with respect to more consistent circular magnetic equilibria as shown in [51] (see Figure 6 from [52] too).

$$\mathbf{n} \cdot \boldsymbol{\Omega}_{\mathbf{J}} = n\omega_{ds} + n\omega_{\mathbf{E}\times\mathbf{B}} + k_\parallel v_\parallel = -(2-\lambda b)\frac{k_\theta T_s}{e_s BR}(\cos\theta + (\hat{s}\theta - \alpha\sin\theta)\sin\theta)\frac{E}{T_s} + \frac{k_\theta E_r}{B} + k_\parallel v_\parallel \tag{4}$$

$\lambda = \frac{\mu B}{E}$ is the pitch-angle and $b(r,\theta) = \frac{B(r,\theta)}{B(r,0)}$ is the magnetic field normalized to its value at the outboard midplane. $\hat{s}$ is the magnetic shear and $\alpha = -q^2\beta\nabla P/P$ is the MHD parameter.

The first term, $n\omega_{ds}$, in (4) corresponds to the curvature and $\nabla B$ drifts whose expression is valid only in the low $\beta$ limit [53] and at lowest order in $\epsilon$[51]. The second term, $n\omega_{\mathbf{E}\times\mathbf{B}} = \frac{k_\theta E_r}{B}$, is the $\mathbf{E} \times \mathbf{B}$ drift and the last term is associated with the fast parallel motion of particles. $k_{\parallel}v_{\parallel}$ expression is given by (5).

$$k_{\parallel}v_{\parallel} = \pm \frac{v_{Ts}x}{qRd}\sqrt{\xi(1 - \lambda b)} \tag{5}$$

where $d = \frac{1}{k_\theta \hat{s}}$ is the distance between resonant surfaces such that $q = m/n$ and $x$, the distance to the closest resonant surface. The curvature and $\nabla B$ drift is expressed as $n\omega_{ds} = (2 - \lambda b)n\bar{\omega}_{ds}f_\theta\xi$ with $f_\theta = \cos\theta + (\hat{s}\theta - \alpha\sin\theta)\sin\theta$ and $\xi = E/T_s$. Overall, (2) reads:

$$\sum_s \frac{e_s^2 n_s}{T_s} \left\langle \left( \left(1 + \frac{2u_{\parallel}v_{\parallel}}{v_{Ts}^2} + \frac{u_{\parallel}^2}{v_{Ts}^2}\left(\frac{2v_{\parallel}^2}{v_{Ts}^2} - 1\right)\right)e^{-\xi}\left(1 - \frac{\omega - n\omega_{E\times B} - \mathbf{n}\cdot\mathbf{\Omega}_s^*}{\omega - \mathbf{n}\cdot\mathbf{\Omega_J} + \imath o^+}\right) J_0^2(k_\perp\rho_s)\left|\tilde{\phi}_{n\omega}\right|^2 \right\rangle = 0 \tag{6}$$

$n\omega_{\mathbf{E}\times\mathbf{B}} = k_\theta E_r/B$ appearing in (6) results from the simplification of $\mathbf{n}\cdot\partial_{\mathbf{J}}E/T_s$ from $\mathbf{n}\cdot\partial_{\mathbf{J}}f_0$ with $\mathbf{n}\cdot\partial_{\mathbf{J}}h_0$. $n\omega_{\mathbf{E}\times\mathbf{B}}$ is species independent so $\omega - n\omega_{E\times B}$ can be replaced by one variable $\varpi$.

One important approximation made in QuaLiKiz is the use of the ballooning representation [54–56] truncated at lowest order i.e. only the lowest harmonic in the infinite sum is retained. In this case, the ballooning representation comes down to an infinite sum of identical modes at $(r_0, n)$ position, $r_0$ being a resonant $q = m/n$ radius ([see 1, App. A.1] or [57]). This enables a local treatment in $r$ at the expense of a limitation on the $\theta$ expansion of the mode to $\theta \in [-\pi; \pi]$ as illustrated in Appendix E. The integration over $\mathbf{J}$ and $\boldsymbol{\alpha}$ then comes down to integration over the pitch-angle, the energy $\xi = \frac{E}{T_s}$ and $k_r$. Indeed, $\theta$ integration is done through $\theta = k_r d$ [55] and axisymmetry allows for Fourier decomposition in the toroidal direction. At this stage, it is important to acknowledge that such an approximation is valid only if the eigenmodes are sufficiently coupled together by the magnetic shear. A condition for that is the mode width w – expressed in Sec. 3.1 – to be much larger than $d$. This is equivalent to say the eigenfunction is peaked and does not expand outside $[-\pi; \pi]$. It was validated down to $\hat{s} = 0.1$ and $k_\theta\rho_s = 0.15$ [see 58, App. C]. In addition, the gradient lengths $L_x$ (among density, temperature, velocity, safety factor) must satisfy:

$$L_x \gg d \tag{7}$$

to ensure that the envelope effects are small. For highly sheared plasma flows, the validity of the approach has to be considered. If the velocity gradient scale length is defined as $L_u = \frac{v_{Ts}}{\nabla u_{\parallel}}$, it can reach values as small as $R/5$ in core tokamak plasmas. The condition (7) then becomes $\epsilon \ll nq\hat{s}/5$ where $\epsilon$ is the inverse aspect ratio. So, for highly rotating plasmas, the approach is valid down to $\hat{s} \geq 0.2$ and $n \geq 10$ which is similar to the limitations seen in [58]. The issue of the ballooning representation compatibility with a poloidal sheared velocity has been extensively studied[24, 59, 60]. Nevertheless,

since (7) is satisfied for experimental values of $L_{\gamma_E} = v_{Ts}/\gamma_E = v_{Ts}B/\frac{dE_r}{dr} > R$, it is considered that modes remain ballooned around $\theta = 0$ and the ballooning representation is used truncated at lowest order.

In QuaLiKiz, the response of trapped and passing particles are separated to take advantage of their different dynamics. An average over the bounce motion is performed for trapped particles, reducing further the numerical cost of the model because it enables the removal of the $\theta$ dependence of the drift frequencies. In the same spirit as the gyromotion average, bounce motion average results in the multiplication of the trapped particles response by Bessel functions $J_m(k_r\delta_s)$, $k_\perp$ coming down to $k_r$ in the thin banana approximation. $\delta_s$ is the banana width of the species $s$. Because of the assumption of local Maxwellian equilibrium, the Bessel functions integration is done separately giving $\mathcal{B}_m(a) = \exp(-a^2)I_m(a^2)$ ([see 1, App.A.4] for the $m = 0$ case). (6) can be written under the condensed form (8), $\mathcal{I}_{s,m,tr}$ and $\mathcal{I}_{s,pass}$ expression being detailed in Appendix B and Appendix A respectively.

$$\sum_s \frac{e_s^2 n_s}{T_s} \left[ 1 - \int \frac{dk_r}{2\pi} \left( \langle \mathcal{I}_{s,pass} \rangle_p \mathcal{B}_0(k_\perp\rho_s) - \sum_m \langle \mathcal{I}_{s,m,tr} \rangle_t \mathcal{B}_0(k_\perp\rho_s)\mathcal{B}_m(k_r\delta_s) \right) \right] = 0 \quad (8)$$

The integration over the passing domain is

$$\langle \cdots \rangle_p = \int_0^\infty \frac{2\sqrt{\xi}}{\sqrt{\pi}} \exp(-\xi)d\xi \int_0^{\lambda_c} \frac{d\lambda}{4\bar{\omega}_b}$$

$\lambda_c = \frac{1-\epsilon}{1+\epsilon}$ is the minimum value of the pitch angle for which particles can be trapped and $\bar{\omega}_b$ is the normalization of $\lambda$ over the parallel (or bounce) motion $\bar{\omega}_b^{-1} = \oint \frac{d\theta}{2\pi} \frac{1}{\sqrt{1-\lambda b}}$ with $\oint = \int_\pi^\pi$ for passing particles and $\oint \approx 2\int_{-\theta_b}^{\theta_b}$ for trapped particles, $\theta_b$ being the bouncing point of the trapped particles. The integration over the trapped domain then reads:

$$\langle \cdots \rangle_t = \int_0^\infty \frac{2\sqrt{\xi}}{\sqrt{\pi}} \exp(-\xi)d\xi \int_{\lambda_c}^1 \frac{d\lambda}{4\bar{\omega}_b} = f_t \int_0^\infty \frac{2\sqrt{\xi}}{\sqrt{\pi}} \exp(-\xi)d\xi \int_0^1 K(\kappa)\kappa d\kappa$$

where $f_t$ is the fraction of trapped particles, $\kappa$ is related to the pitch-angle via $\lambda = 1 - 2\epsilon\kappa^2$ and $K$ is the complete elliptic integral of the first kind. For the expression of $\mathcal{I}_{s,pass}$ and $\mathcal{I}_{s,tr}$ please refer to Appendix A and Appendix B where the algebra is detailed.

In short, with the definitions given in Appendix A and Appendix B, the expression (8) can be written as

$$\sum_s \frac{n_s e_s^2}{T_s} \left( 1 - \mathcal{L}_{s,pas}(\omega) - \mathcal{L}_{s,tr}(\omega) \right) = 0 \quad (9)$$

In this section, the linearized gyrokinetic dispersion relation (9) at the heart of the linear solver of QuaLiKiz was derived including the effect of the non-zero values for $u_\parallel$, $\nabla u_\parallel$ and $\mathbf{E} \times \mathbf{B}$ shift in the low Mach number approximation and other standard approximations for QuaLiKiz, namely low $\beta$ (electrostatic), large aspect ratio and lowest

order ballooning representation. The detail of the various functionals is available in Appendix A and Appendix B. To solve this eigenfunction/eigenvalue equation, the eigenfunction $\tilde{\phi}$ is calculated in the analytic fluid limit, which is revisited in the following section to include the effect of sheared flows.

## 3. Analytic eigenfunction calculation

In QuaLiKiz, the eigenmodes are not self-consistently calculated from (9). To gain CPU time – 2 orders of magnitude together with the dimension reduction associated with the ballooning approximation detailed in previous section – they are calculated in the fluid limit in which (9) can be solved analytically. This method proved to give satisfactory results compared to self-consistent gyrokinetic calculations in the case with no rotation (see in particular [58, Appendix C] and [34, Appendix A]). A model for analytic eigenfunctions in presence of sheared flows is derived in this section. It is shown that shifted Gaussians are satisfactory approximates of the gyrokinetic eigenfunctions in that case. A comparison against GKW[40] is performed as a validation for the cases with rotation.

   Fluid modeling of the linear eigenmode equation to find an analytic solution for the eigenfunction is not a new idea[18, 61–65]. Here, the derivation is performed in the toroidal geometry and include the effects from $u_\parallel$, $\nabla u_\parallel$ and the $\mathbf{E} \times \mathbf{B}$ shear. (9) being the starting point of this derivation, all previous approximations still apply in particular the low Mach number approximation and the ballooning representation at lowest order.

### 3.1. Description of the fluid model

The fluid limit approximation consists in considering events sufficiently fast decorrelated by collisions such that $\varpi = \omega - n\omega_{E \times B} \gg \bar{\omega}_{di}$ and $\varpi \gg k_\parallel v_{\parallel i}$. This approximation enables the development of the dispersion relation given in (9)in power of the small quantities $\frac{\omega_{ds}}{\varpi}$, $\frac{k_\parallel v_\parallel}{\varpi}$ and obtain a polynomial expression in $\varpi$ as detailed in (D.1).

   For short wavelengths: $k_\perp \rho_i < 1$, the Bessel functions can be linearized such that $\mathcal{B}_0(k_\perp \rho_i) \approx 1 - \frac{k_\perp^2 \rho_i^2}{2}$. At this spatial scale, events are sufficiently slow such that $\omega \ll k_\parallel v_{\parallel e}$. Passing electrons are then considered adiabatic. In contrast, TEM space and time scales being the same as ions modes, trapped electrons are treated by the model. Since $k_r \delta_e < k_r \rho_i < 1$, the Bessel functions on trapped electrons are considered close to unity $\mathcal{B}_0(k_r \delta_e) \approx 1$. For trapped ions, the finite banana width effects are expended in power of $k_r$ too: $\mathcal{B}_0(k_r \delta_i) \approx 1 - \frac{k_r^2 \delta_i^2}{2}$. The resulting polynomial expression for the eigenmode is given in (D.1).

   As explained in detail in Appendix D, the electroneutrality condition $\sum_s e_s n_s = 0$ is used to reformulate (D.1). It enables a species independent normalization frequency $n\bar{\omega}_d = n\bar{\omega}_{de} = -T_e/T_i n\bar{\omega}_{di}$. An inverse Fourier transform $k_r \to -\imath \partial_x$ is performed leading to a second order differential equation. $\varpi$ is replaced with $\omega - n\omega_{\mathbf{E} \times \mathbf{B}}$ because $n\omega_{\mathbf{E} \times \mathbf{B}}$ has an $x$ dependence in case of $\mathbf{E} \times \mathbf{B}$ shear. The radial electric field is considered

smooth enough such that it can be linearized into $E_r \rightarrow E_{r0} + E'_r x + O(x^2)$ implying the linearization of $n\omega_{\mathbf{E}\times\mathbf{B}}$ in $x$: $n\omega_{\mathbf{E}\times\mathbf{B}} = n\omega_{E0} + k_\theta \gamma_E x + O(x^2)$. Therefore, only the linear terms in $\gamma_E x$ are taken into account in the eigenmode equation. The details of the derivation of the eigenmode equation are detailed in Appendix D. Its final expression is given by (10).

$$\left[ \left( \omega \left( \frac{d_{\text{eff}}^2}{2} \frac{\mathrm{d}^2}{\mathrm{d}x^2} - \frac{k_\theta^2 \rho_{\text{eff}}^2}{2} \right) + \frac{k_\parallel'^2 c_{\text{eff}}^2}{2\omega} x^2 \right) (\omega - n\omega_{pi}^*) - 2n\bar{\omega}_d(\omega - k_\theta\gamma_E) - \omega^2 + 2k_\theta\gamma_E + \right.$$

$$\left. (\omega - k_\theta\gamma_E)\, n\omega_{ne}^* - \frac{f_t}{f_p} n\omega_{pe}^* n\bar{\omega}_d + k_\parallel' c_{\text{eff}} \left( n\omega_u^* + \frac{u_\parallel}{c_{\text{eff}}} \left( \frac{Z_{\text{eff}}}{\tau}\omega + n\omega_{ne}^* - 8n\bar{\omega}_d \right) \right) x \right] \tilde{\phi} = 0$$

(10)

The solution of this linear second order differential equation is a shifted Gaussian:

$$\tilde{\phi} = \frac{\phi_0}{(\pi\Re(\mathrm{w}^2))^{1/4}} \exp -\frac{(x - \mathrm{x}_0)^2}{2\mathrm{w}^2}$$

(11)

This solution is characterized by two quantities:

- The *mode width* w determined by: $\mathrm{w}^2 = \dfrac{-\imath\omega d_{\text{eff}}}{|k_\parallel'|c_{\text{eff}}}$, $\omega$ being the self-consistent solution of (10). The mode width therefore depends on $\gamma_E$, $n\omega_u^*$ and $u_\parallel$ through $\omega$. Note that $\mathrm{w}^2$ was previously calculated with an interchange ansatz for $\omega$ in QuaLiKiz considering w real, it is defined here to cancel the quadratic terms in $x$ in (10);

- The *mode shift* $\mathrm{x}_0$ characterizing the parallel asymmetrization of the mode expressed by:

$$\mathrm{x}_0 = \frac{2n\bar{\omega}_d}{\omega - \omega_{ne}^*} \frac{\frac{q}{s}\gamma_E^N(2\omega + 2n\bar{\omega}_d - n\omega_{ne}^*) + n\omega_u^* + \frac{u_\parallel}{c_{\text{eff}}}\left(\frac{Z_{\text{eff}}}{\tau}\omega + n\omega_{ne}^* - 8n\bar{\omega}_d\right)}{k_\parallel' c_{\text{eff}}}$$

(12)

where $\gamma_E^N = \frac{\gamma_E}{c_{\text{eff}}/R}$ corresponds to usual normalizations of the $E\times B$ shear. The approach taken here to include consistently the effect of the $E\times B$ shear in the linear eigenfunctions is quite different than what is used in GLF 23/TGLF [20, 66] where the eigenfunctions do not include the asymmetrization due to $\gamma_E$.

The ITG dispersion relation $\frac{\omega}{\omega-\omega_{pi}^*} = -\frac{2n\bar{\omega}_d}{\omega-\omega_{ne}^*}$ was used in (12) to ensure that the shift stays small according to the assumption that the turbulence is ballooned around $\theta = 0$ in the same spirit as what is done in [63]. It is otherwise determined to cancel to linear terms in $x$ in (10) As $\mathrm{x}_0$ is complex, an imaginary shift in $x$ corresponds to a real shift in $k_r$ which means a *linear* stabilization of large radial structures. Strong dependencies of the Gaussian shift are on:

- $\mathbf{E}\times\mathbf{B}$ shear through the "$\gamma_E^N$" term;
- the parallel velocity gradient through the "$n\omega_u^*$" term;
- the parallel velocity through the "$u_\parallel$" term.

These dependencies are detailed and compared to GKW self-consistent solutions in the next section.
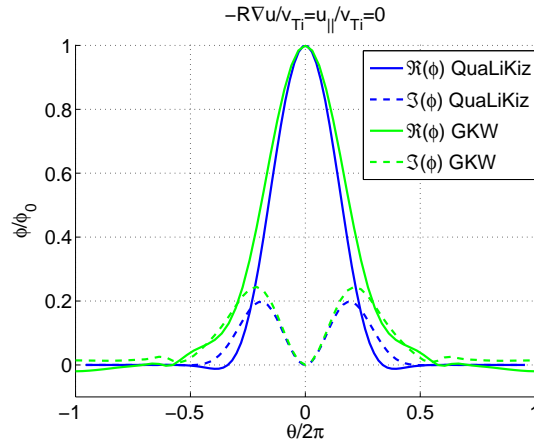
**Figure 1.** Parallel structure of the eigenfunctions showing null $k_\parallel$ at zero rotation. GA-std parameters, $k_\theta \rho_s = 0.3$

## 3.2. Linear eigenfunctions validation

Now that the model employed to predict the linear eigenfunctions has been described, it remains to be compared to self-consistent gyrokinetic eigenfunctions. This comparison is realized with the linear version of the GKW code [40] which uses a $\delta f$ decomposition of the distribution function like QuaLiKiz. Field aligned coordinates [67] are employed rather than the ballooning representation. There are no approximation in the integration over the pitch-angle and the energy and various magnetic equilibria are available in GKW. For consistency with QuaLiKiz, all direct comparisons are realized with the $\hat{s} - \alpha$ equilibrium in GKW using $\alpha = 0$. In this equilibrium, GKW parallel coordinate $s$ is equivalent to QuaLiKiz $\frac{\theta}{2\pi}$[40]. The effects of the parallel velocity and its gradient are shown to be correctly accounted for in QuaLiKiz. The effect of $\gamma_E$ is studied as well.

First, it is verified in Figure 1 that the new model previously presented gives a satisfactory agreement with gyrokinetic eigenfunctions in the absence of rotation as in [34, 58]. Both GKW (in light green) and QuaLiKiz eigenfunctions (in darker blue) are plotted as a function of the parallel label $\theta/(2\pi)$. GA-std parameters are used. Unless stated otherwise $\epsilon = 1/6$, $R/L_n = 3$, $R/L_T = 9$, $q = 2$, $\hat{s} = 1$, $Z_{eff} = 1$. The poloidal wave number for the study is $k_\theta \rho_s = 0.3$ as it roughly corresponds to the spectral peak of non-linear fluxes. Figure 1 shows a good match between QuaLiKiz trial eigenfunctions and GKW. QuaLiKiz eigenfunction is more peaked around $\theta = 0$ traducing a slight overestimation of the mode width. This is consistent with Figure 16 from [58].

The influence of the parallel rotation on the parallel structure of the eigenmodes is now studied in Figure 2. In the left panel, QuaLiKiz and GKW eigenfunctions are plotted against $s = \theta/2\pi$ with GA-std parameters except the parallel velocity gradient (PVG) set to $-4v_{Ti}/R$. This corresponds to maximum experimental values of PVG in core tokamak plasmas[9, 19]. In the right panel, the PVG is null and the parallel velocity is set to $0.2v_{Ti}$. It corresponds to the standard rotation of core plasmas. In both panels, the eigenfunctions appear ballooned in the region where $\theta \sim 0$ confirming
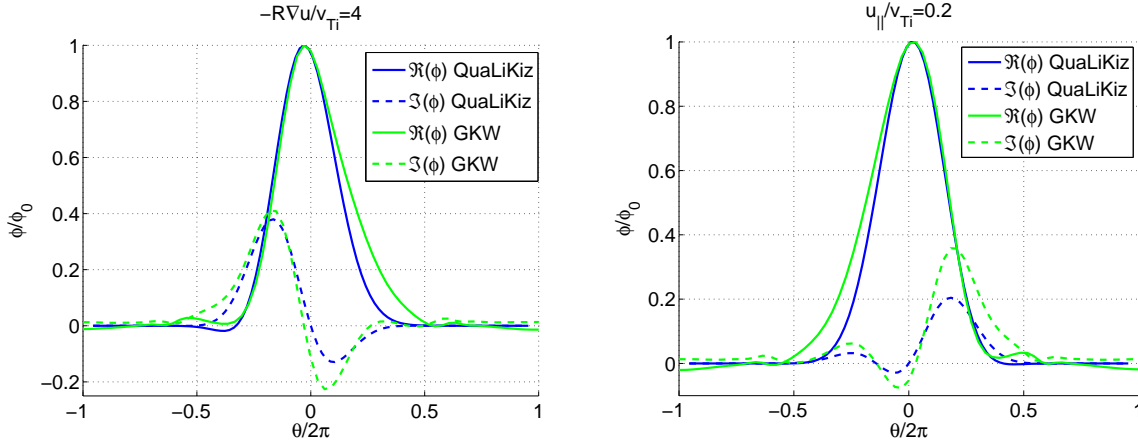
**Figure 2.** Parallel structure of the eigenfunctions showing finite $k_\parallel$ in presence of finite $\nabla u_\parallel$ (left) and $u_\parallel$ (right)
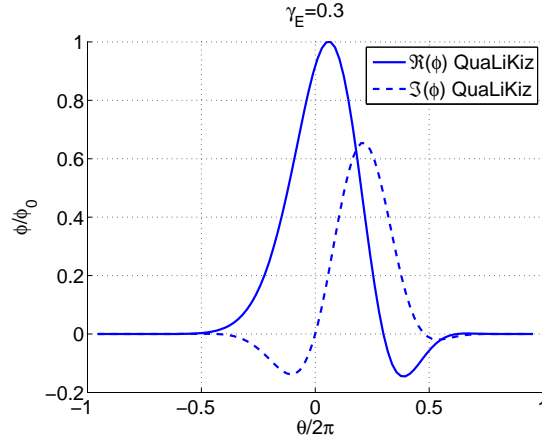


**Figure 3.** Parallel structure of the eigenfunctions showing finite $k_\parallel$ in presence of finite $\mathbf{E} \times \mathbf{B}$ shear

previous approximations. But, contrary to the case where there is no rotation [58] (see Figure 1), the eigenfunctions are no longer $\theta$-symmetric. As expected from the expression (12) for the mode shift, $x_0$ is proportional to $u_\parallel$, $\nabla u_\parallel$ and $\gamma_E$. The agreement with gyrokinetic eigenfunctions is very good in these conditions for both the real and the imaginary parts. The existence of an imaginary part is a novelty. It was previously neglected since, in the absence of sheared flows, the imaginary part of the mode width is small compared its real part and there is no shift in this case (see Figure 1). It was included here because it becomes of the order of the real part in case of strong $\mathbf{E} \times \mathbf{B}$ flow shear. An example of the eigenfunctions found in presence of $\mathbf{E} \times \mathbf{B}$ shearing is plotted in Figure 3 where the imaginary part $\Im(\phi)$ (dashed curve) is found to be comparable to the real part $\Re(\phi)$ of the eigenfunction. The $\theta$-shift of the real part of $\tilde{\phi}$ is especially important because it represents a $k_\parallel$-shift contributing to the momentum flux as shown in Sec. 5. For $\mathbf{E} \times \mathbf{B}$ shear, there is no direct comparison possible, since the general solutions of the linearized gyrokinetic equation in such conditions are oscillating Floquet

modes[24, 59]. In the reduced model presented here, eigenfunctions are found thanks to the truncation at lowest order of the ballooning representation.

With the GA-std case set of parameters, chosen for the cases presented above, Ion Temperature Gradient (ITG) modes are dominant. They are known to be ballooned around $\theta = 0$ in ballooning space [57] so the approximations taken in Sec. 2 is correct. The case of Trapped Electron eigenmodes (TEM) is briefly discussed now and in more detail in Appendix E. TEM are more extended in $\theta$ than ITG modes[68]. Taking only the lowest term of the ballooning representation as is done in QuaLiKiz, fails to reproduce modes presenting an extension in ballooning space larger than $\theta \in [-\pi; \pi]$ which is especially the case for strongly dominant TEM at $k_\theta \rho_s \sim 1$. This leads to the overestimation of the TEM stability in this spectral range as illustrated in Figure 5 by QuaLiKiz underestimation of the growth rates compared to GKW. For transport studies however, the low $k_\theta \rho_s$ matter most and the quasi-linear approximation is only valid at low $k_\theta \rho_s$ [see 58]. This induces that QuaLiKiz is able to model correctly TEM dominated regimes as illustrated by Figure 9 of [3].

To summarize, the effects of $u_\parallel$, $\nabla u_\parallel$ and $\mathbf{E} \times \mathbf{B}$ shear are included in the model presented in Sec. 3.1. They result in a complex shift of the Gaussian eigenfunction and an increase of the relative amplitude of its imaginary part. The influence of $u_\parallel$ and $\nabla u_\parallel$ is successfully benchmarked against GKW. QuaLiKiz model represents correctly ITG dominated eigenmodes but it cannot capture the extension outside $|\theta| = \pi$ of TEM. This is a necessary trade off to gain two orders of magnitude in CPU time with respect to self-consistent gyrokinetic eigenfunctions calculation making QuaLiKiz suitable for integrated modeling.

## 4. Impact of sheared flows on linear growth rates

A way to validate the model developed in Sec. 2 and 3 is to compare the linear growth rates $\gamma = \Im(\omega)$ found with QuaLiKiz against the results from a gyrokinetic code which does not use the simplifications previously detailed. An important benchmark effort has already been done, comparing QuaLiKiz growth rates against GS2 [1, 34] and GENE[58]. The comparison is limited here to the sheared flows impact by varying $u_\parallel$, $\nabla u_\parallel$ and $\gamma_E$ using GKW linear simulations and GA-standard based test cases. Unless stated otherwise $\epsilon = 1/6$, $R/L_T = 9$, $R/L_n = 3$, $q = 2$, $\hat{s} = 1$, $\alpha = 0$, $\nu^* = 0$ in this section. The parallel velocity gradient destabilization and the stabilizing effect of $\mathbf{E} \times \mathbf{B}$ shear are successfully benchmarked. The effects of the parallel velocity are recovered within the range of validity of the low Mach number approximation.

### 4.1. Parallel velocity gradient instability with $\nabla u_\parallel$

First, let us concentrate on $\nabla u_\parallel$. It has been extensively reported in the literature that parallel velocity gradients (PVG) destabilize a Kelvin-Helmholtz like instability[17, 19, 63]. PVG instabilities are destabilized by velocity gradients at rather high values
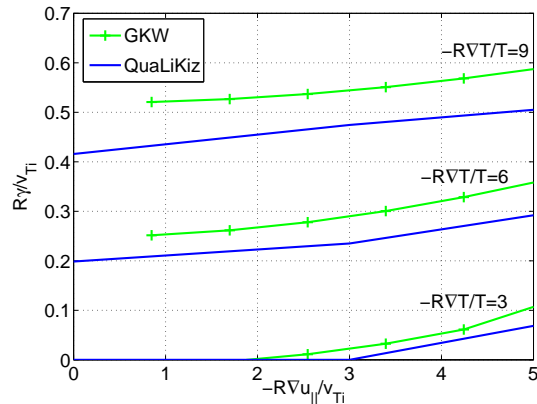
**Figure 4.** Maximum linear growth rates from QuaLiKiz and GKW for GA-std parameters

$\frac{R\nabla u_\parallel}{v_{Ti}} \approx 5$ compared to the experiments[19]. But its threshold is reduced with increasing temperature gradient so that it can destabilize otherwise marginally stable conditions for ITG turbulence. Finally, PVG is known for enhancing the growth rates of already unstable ITG modes. All these effects are presented in Figure 4 where a scan in $\nabla u_\parallel$ is performed up to $\nabla u_\parallel = -5v_{Ti}/R$ for 3 values of temperature gradients $R/L_T = \{3, 6, 9\}$. For flatter temperature profile conditions ($R/L_T = 3$), which is linearly stable without rotation, the PVG destabilization threshold is recovered. For the peaked temperature profile condition ($R/L_T = \{6, 9\}$), which are ITG unstable without rotation, the growth rate inflation with $\nabla u_\parallel$ is captured by QuaLiKiz. The values of the growth rates are nevertheless slightly underestimated.

*4.2. Impact of $u_\parallel$*

The parallel velocity is known to have opposite effects on ions and electrons modes. It stabilizes ITG modes and destabilizes trapped electron modes (TEM) via the expansion of the trapped domain in velocity space with increasing $u_\parallel$[52, 69]. These effects are studied in Figure 5. Simulations from QuaLiKiz (in plain curve) and GKW (in dashed curve) based on GA-std parameters are represented. The parallel velocity is varied from 0 to $0.6v_{Ti}$, a larger value than usually observed in high aspect ratio tokamak core plasmas[9]. The effect of the low Mach number approximation – used in QuaLiKiz, not in GKW – is analyzed.

When comparing GKW (with centrifugal effects) and QuaLiKiz, Figure 5(b), it is clear that ITGs are stabilized in both codes but TEMs are not destabilized in QuaLiKiz. This discrepancy is due to the low Mach number approximation which does not retain centrifugal effects. They were removed in GKW in Figure 5(a) to illustrate this. Indeed, without centrifugal effects, GKW electron modes are not destabilized. Moreover, at higher $\frac{u_\parallel}{v_{Ti}}$ values, ITGs are overstabilized in QuaLiKiz and TEMs become dominant for lower $k_\theta \rho_s$ values as $u_\parallel$ increases due to the stabilization of ITGs. This is a consequence
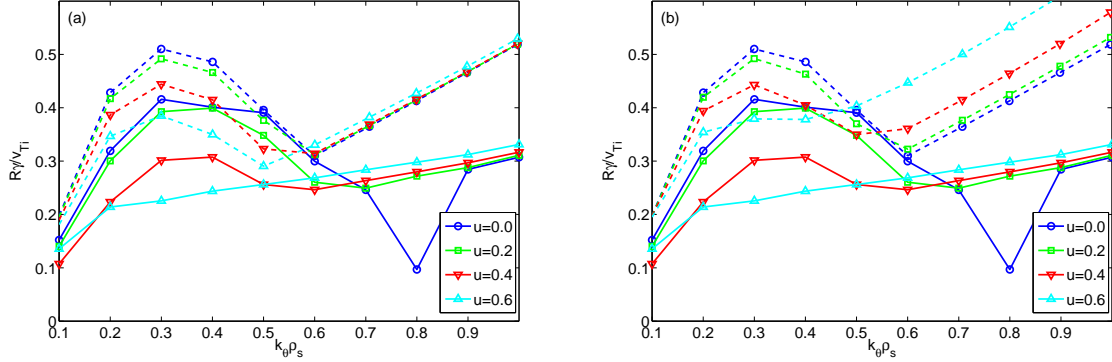
**Figure 5.** Linear growth rates from QuaLiKiz (plain curves) and GKW (dashed) for GA-std based cases with various $u = \frac{u_\parallel}{v_{Ti}}$ values. (a) GKW run without centrifugal effects (b) GKW run with centrifugal effects

of the development up to second order in $u_\parallel$ of the equilibrium distribution function (see Equation 6) which underestimates the values of the exponential in $u_\parallel$ contained in $f_0$ definition at larger values of $v_\parallel$. The underestimation of TEM growth rates by QuaLiKiz at higher $k_\theta \rho_s$ for any values of $u_\parallel$ is related to a discrepancy between QuaLiKiz and GKW eigenfunctions as detailed in Appendix E.

### 4.3. Stabilization by $\mathbf{E} \times \mathbf{B}$ shear

The extensively studied stabilization of the turbulence by $E \times B$ shear [5, 24, 27, 31, 62, 70, 71] is addressed in this section. To be able to perform the comparison with GKW, we highlight that a new method to calculate effective growth rates for initial value codes such as GKW with $\mathbf{E} \times \mathbf{B}$ shear is developed. This method is close to that of [72] and results in a better qualitative agreement with non-linear observations. Indeed, with finite $\mathbf{E} \times \mathbf{B}$ shear, Floquet modes are solutions of the linearized gyrokinetic equation, composed of an exponentially growing part and an oscillating part. Consequently, when averaging over the entire temporal window of the simulation, a strong drop in the effective growth rate is observed for the first non-zero value of $\gamma_E$ and then a weak dependence with $\gamma_E$ is seen as explained in [24] and represented in Figure 7 dashed curve. In contrast, non-linear simulations show a smooth reduction of the fluxes with increasing $\mathbf{E} \times \mathbf{B}$ shear[73], fitted at times by a linear quench rule[24]. An explanation for this discrepancy is that the non-linear decorrelation time is shorter than the time over which one averages the growth rates. The method proposed here to resolve this issue can be decomposed in two steps illustrated by Figure 6.

- First, an effective growth rate $\gamma_{eff}(t)$ is calculated on 3 decorrelation times $\tau_{NL}$ considering that $\tau_{NL} = \gamma_{eff}^{-1}$. It means that $\gamma_{eff} = \left( \ln(\phi(t + \Delta t)) - \ln(\phi(t)) \right) / \Delta t$ is calculated with $\Delta t = 3/\gamma_{eff}$. Equivalently $\phi(t + \Delta t) = \exp(3)\phi(t)$. The corresponding $\Delta t$ is represented by the shaded area in Figure 6;

- The time window corresponding to $3\tau_{NL}$ is then moved along the simulation as
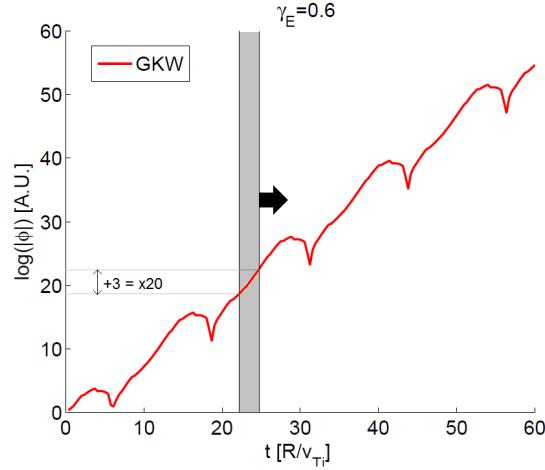
**Figure 6.** Example of the time evolution of a Floquet mode from a GKW simulation at $R/L_T = 15$, $\gamma_E = 0.6$ and other parameters from GA-std. The shaded region corresponds to $3\gamma^{-1} \approx 3\tau_{NL}$. The black arrow represents the displacement of the shaded region along $t$.

indicated by the black arrow in Figure 6. The effective growth rate of the entire simulation is taken to be the $3^{rd}$ quartile of the ensemble of $\gamma_{eff}[0; t_{end}]$ to remove all the negative $\gamma_{eff}(t)$ from the statistics.

This method is compared to the standard one – see for example [31] – in Figure 7. The so-called "GKW mean value" dotted curve represents the usual method and the "GKW" plain curve with error bars represents the method described above. The error bars extent corresponds to one standard deviation around the $3^{rd}$ quartile value. The usual "jump" in $\gamma$ from 0 to finite value of $\gamma_E$ is reduced, resulting in better qualitative agreement with the results from non-linear simulations. The growth rates from the eigenvalue code QuaLiKiz are plotted on the same figure in plain curve for comparison. They are in agreement with $\gamma_{eff}$ within the error bars of the method presented above. This result shows that the $\mathbf{E} \times \mathbf{B}$ stabilization mechanism is captured by QuaLiKiz approach using fluid shifted Gaussian eigenfunctions without any fitting parameter contrary to the quench rule usually used in transport codes [20, 66].

Through the three examples presented above, QuaLiKiz linear growth rates evolution with the three relevant quantities for sheared flows in a tokamak plasmas – $u_\parallel$, $\nabla u_\parallel$ and $\gamma_E$ – have been validated. Along with the correct linear eigenfunctions, this gives the possibility to make a quasi linear estimate of the turbulent heat, particle and momentum fluxes accounting properly for PVG and $\mathbf{E} \times \mathbf{B}$ shear stabilization at lower CPU cost.
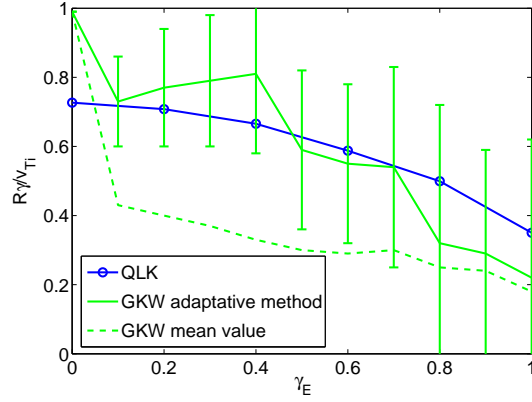
**Figure 7.** Maximum QuaLiKiz growth rates and GKW effective growth rates calculated with the standard averaging method and a new statistical method

## 5. Quasi-linear fluxes

Quasi-linear models are extensively used to predict heat, particle and momentum fluxes without the numerical cost of non-linear simulations[3, 21, 26, 74–77]. They have been heavily benchmarked against non linear simulations for heat and particles [78–80] and more recently for momentum[22]. In this section the quasi-linear momentum flux is derived in QuaLiKiz formalism. In 5.1 the linear response is shown to be similar to the expressions of $\mathcal{L}_{s,\text{pass}}$ and $\mathcal{L}_{s,\text{tr}}$ of the linearized gyrokinetic equation (2). Indeed, in the quasi-linear approximation, the fluxes can be written as derived in App. A of [2]:

$$\Gamma = \sum_{\mathbf{n},\omega} \mathbf{n} \cdot \Im \left( \frac{\mathbf{n} \cdot \partial_{\mathbf{J}} f_0}{\omega - \mathbf{n} \cdot \mathbf{\Omega_J} + \imath o^+} \right) |\tilde{h}_{\mathbf{n}\omega}|^2 \tag{13}$$

$|\tilde{h}_{\mathbf{n}\omega}|^2$ corresponds here to the saturated potential. This potential cannot be self-consistently determined since there is no saturation mechanism embedded in the theory. It must be constructed based on experimental observations and non-linear simulations[2, 3]. In QuaLiKiz, the saturated potential maximum is defined by a mixing length rule discussed in Sec. 5.2. The saturated potential spectrum in $k_\perp$ is also reviewed in Sec. 5.2. The results are compared against non-linear GKW simulations in 5.3. The $\mathbf{E} \times \mathbf{B}$ shear quenching of the particle and heat fluxes is recovered. The associated momentum fluxes match for small values of $\mathbf{E} \times \mathbf{B}$ shear $\gamma_E^N < 0.1$ but overestimated in QuaLiKiz by a factor 2 for larger values of $\gamma_E$. Finally the influence of $u_\parallel$ and $\nabla u_\parallel$ on QuaLiKiz momentum flux is validated by calculating the Prandtl and pinch numbers.

### 5.1. Quasi-linear momentum flux in QuaLiKiz formalism

As indicated in (13), quasi-linear fluxes are composed of two parts. One is a linear response and the other is the saturated potential. The linear response is detailed here. In an axisymmetric tokamak, the flux surface averaged *toroidal* momentum

flux is the quantity to calculate since the flux surface averaged angular momentum $p_\phi = \int mRv_\phi \tilde{f} \mathrm{d}^3 v$ is globally conserved[81]. Here its perpendicular part is neglected and only the *parallel* contribution is retained. Moreover, $R$ used in the definition of the momentum flux $\Pi_\parallel$ is the major radius at the magnetic axis. There is therefore no $\epsilon$ correction of this quantity. The momentum flux calculated in QuaLiKiz is defined as follows:

$$\Pi_\parallel = \sum_s \Re \left\langle m_s R v_\parallel \tilde{f}_s \frac{\imath k_\theta \tilde{\phi}}{B} \right\rangle \tag{14}$$

$\tilde{f}_s = \frac{\mathbf{n} \partial_\mathbf{J} f_0^s}{\omega - \mathbf{nn} \cdot \mathbf{\Omega_J} + \imath o^+} \tilde{h}$ is the perturbed distribution function determined by the linearized Vlasov equation and $\langle \cdots \rangle$ means integration over the velocity space. $\Pi_\parallel$ is positive for an outward flux of momentum in the direction of $\mathbf{B}$. Using the formalism developed in Sec. 2, the complete expression of $\Pi_\parallel$ is presented in (C.1) by replacing $\tilde{f}_s$ with its expression given in Appendix C (6).

Apart from the saturated potential $\tilde{\phi}_{n\omega}$, the expression (6) is similar to the linear gyrokinetic response presented in Sec. 2 except that only the imaginary part is of interest for the flux and that the integrations over $(\xi, \lambda)$ are slightly different due to the multiplication by $v_\parallel = \pm v_{Ts} \sqrt{\xi(1 - \lambda b)}$. The same techniques as before are then employed. The contributions from trapped and passing particles to the momentum flux are treated separately. The expression for $\mathcal{J}_{s,pass}$ is detailed in (C.3). Note that the parity of (C.3) is opposite to that of (A.2) due to the multiplication by $v_\parallel$. This guarantees that without rotation the momentum is zero. For trapped particles, the multiplication by $v_\parallel$ implies there is no contribution to the momentum flux at lowest order in $\epsilon$. However, when expanding up to first order in $\sqrt{\epsilon}$, there is a net contribution from trapped particles, detailed in (C.4).

Given the expressions of the passing and trapped particle contributions to the momentum flux, (C.2) can formally be written in the form:

$$\Pi_\parallel = \sum_s m_s n_s R(-\chi_\parallel \nabla u_\parallel + V_\parallel u_\parallel) + \Pi_{RS} \tag{15}$$

$\chi_\parallel$ representing the momentum diffusivity, $v_\parallel$, the momentum pinch and $\Pi_{RS}$ being the residual stress. However, the identification of $\chi_\parallel$, $V_\parallel$ and $\Pi_{RS}$ with (C.1) is not as straightforward as it may appear. From (C.3) and (C.4), it is clear that $\Pi_\parallel$ contains terms directly proportional to $u_\parallel$ and $\nabla u_\parallel$. They are called $\Pi_u$ and $\Pi_{\nabla u}$. They do not contain all contributions from $u_\parallel$ and $\nabla u_\parallel$. The remaining terms are proportional to the linear eigenfunction shift $x_0$ which, itself, is proportional to $\nabla u_\parallel$, $u_\parallel$ and $\gamma_E$ as expressed by (12) from Sec. 3[64]. These terms proportional to the eigenfunction shift are called $\Pi_{x0}$. If $\mathbf{E} \times \mathbf{B}$ shear is the only symmetry breaker, $\Pi_{x0} \equiv \Pi_{RS}$. Otherwise, $\Pi_{x0} \propto u_\parallel, \nabla u_\parallel, \gamma_E$ cannot be identify with $\Pi_{RS}$ as $\Pi_{\nabla u}$ (resp. $\Pi_u$) does not contain all conductive (resp. convective) contributions to the momentum flux.

The different contributions can be separated by linear regressions. Since we are searching for three unknowns, three simulations are performed with the same set of parameters except for $u_\parallel$, $\nabla u_\parallel$ and $\gamma_E$. The first one is the test simulation. The second

one is performed with the parallel velocity modified by $\pm 20\%$. Both the parallel velocity gradient and the $\mathbf{E} \times \mathbf{B}$ shearing are affected by this modification of the parallel velocity. The last simulation is performed with the parallel velocity *incremented* by $\pm 0.05 v_{Ti}$. The parallel velocity gradient is not perturbed by this modification. Considering that such modifications have a *linear* effect on the momentum flux, a linear regression is possible to estimate the momentum diffusivity $\chi_\parallel$, the pinch $V_\parallel$ and the residual stress $\Pi_{RS}$. If $\Pi_1$ is the parallel momentum flux from the 1$^{\text{st}}$ simulation, $\Pi_2$ from the 2$^{\text{nd}}$ and $\Pi_3$ from the 3$^{\text{rd}}$, and under the assumption that the changes presented above induce only a linear modification, they read:

$$\Pi_1 = \sum_s m_s n_s R(-\chi_\parallel \nabla u_\parallel + V_\parallel u_\parallel) + \Pi_{RS} \tag{16a}$$

$$\Pi_2 = \sum_s m_s n_s R(-1.2 \chi_\parallel \nabla u_\parallel + 1.2 V_\parallel u_\parallel) + \Pi_{RS} \tag{16b}$$

$$\Pi_3 = \sum_s m_s n_s R(-\chi_\parallel \nabla u_\parallel + V_\parallel(u_\parallel + 0.05 v_{Ti})) + \Pi_{RS} \tag{16c}$$

The system (16) is a set of 3 independent equations of 3 variables. Therefore each of the variables $\chi_\parallel$, $V_\parallel$ and $\Pi_{RS}$ is uniquely defined. Varying $u_\parallel$ by $\pm 20\%$ and incrementing $u_\parallel$ by $\pm 0.05 v_{Ti}$ defines 3 different sets of equations. If the momentum flux dependence with respect to $u_\parallel$ and $\nabla u_\parallel$ is linear the 3 systems should give the same results. In the opposite case, the dispersion between the results (inversely) measures the validity of the bilinear regression. The method ensures that linear dependencies of $\gamma_E$ with $\nabla u_\parallel$ and $u_\parallel$ are removed from the residual stress and accounted for in $\chi_\parallel$ and $V_\parallel$ respectively.

The comparison between the direct separation and the 3-point method gives an estimate of the importance of the eigenfunction contribution to the conductive and convective part of the momentum flux as discussed in detail and evaluated in Sec. 5.3. Concerning the residual stress, it corresponds to the momentum flux induced by the parallel symmetry breakers other than $u_\parallel$ and $\nabla u_\parallel$. In QuaLiKiz, only the $\mathbf{E} \times \mathbf{B}$ shearing induced residual stress is calculated. Indeed, the global effects from turbulence intensity gradient [39] or profile shearing [37] are not included. They produce a residual stress of the same order as $\mathbf{E} \times \mathbf{B}$ shearing by tilting the ballooned structure of the turbulence around $\theta_0 \neq 0$ [38].

### *5.2. Saturated potential*

The saturated potential is constructed according to experimental observations and non-linear simulations[2, 3, 82]. The frequency spectrum is a Lorentzian of width $\gamma$ as explained in [2]. In cases of simulations with large $\mathbf{E} \times \mathbf{B}$ shear, the width is modified. Indeed, if $\gamma_E > \gamma$, the shear rate defines a shorter time scale than the linear growth rate. The following rule is therefore: the width of the Lorentzian is $\max(\gamma(k), \gamma_E)$. This rule would need to be validated by non-linear gyrokinetic simulations. It implies a high resolution diagnostic for the frequency that deals correctly with the implementation of the $\mathbf{E} \times \mathbf{B}$ shear. To our knowledge, such a diagnostic does not exist yet.

For the perpendicular wave number spectrum, it was found that a $k_\perp^{-3}$ spectrum reproduces the cascade towards smaller scales found in non-linear simulations and experimentally measured[3]. With such a spectrum, wave numbers higher than $k_\theta \rho_s = 1$ will have little influence on the transport level. Indeed, the significant contributions to the turbulent fluxes found in some non-linear simulations at higher wave numbers [83] depart from the estimation of a saturation rule which is used here. Therefore, the wave number range is kept between $k_\theta \rho_s = 0.05$ and $k_\theta \rho_s = 1$ in the simulations although there is no intrinsic limitation of the maximum perpendicular wave number computable in QuaLiKiz. For the inverse cascade at larger scales, Figure 8 illustrates that a linear spectrum reproduces better non-linear simulations than the $k_\perp^3$ spectrum previously employed.

It should also be noted that all unstable modes (ITGs and TEM) are taken into account in QuaLiKiz and not only the dominant mode. The fluxes are made of the sum of all unstable mode contributions. For each unstable mode, a mixing length rule estimate is used to evaluate its quasilinear weight in the fluxes such that there is no free parameters involved. A mixing length rule estimate on the most unstable mode is used to fix the wave number at which the saturated potential is maximum:

$$\max\left(D_{\text{eff}}(k_\perp) \approx \frac{R\Gamma_s}{n_s}\right) = \frac{k_\theta e_s R}{B}T_s|\tilde{\phi}_n|^2\bigg|_{k_{\max}} = \max\left(\frac{\gamma}{\langle k_\perp^2 \rangle}\right) \tag{17}$$

The expression for $\langle k_\perp^2 \rangle$, based on the idea proposed in [76], has been recently revisited in [58] to improve QuaLiKiz fluxes estimation at low magnetic shear. It reads:

$$\langle k_\perp^2 \rangle = k_\theta^2 + k_r^2 = k_\theta^2 + \left(\sqrt{k_\theta^2 \hat{s}^2 \langle \theta^2 \rangle} + \frac{0.4\exp(-2\hat{s})}{\sqrt{q}} + 1.5(k_\theta - 0.2/\rho_s)H(k_\theta - 0.2/\rho_s)\right)^2 \tag{18}$$

The expression of $k_r$ in QuaLiKiz mixing length rule was modified because it was found that, at low magnetic shear, $k_r^2 = k_\theta^2 \hat{s}^2 \langle \theta^2 \rangle$ resulting from the magnetic field lines shearing is underestimated with respect to non-linear $k_r$ [see 58, Sec. IV C.]. The factor $\frac{0.4\exp(-2\hat{s})}{\sqrt{q}}$ was found to represent best the non linear isotropization at low magnetic shear. Finally, the term $1.5(k_\theta - 0.2/\rho_s)H(k_\theta - 0.2/\rho_s))^2$ ($H$ is the Heaviside function) is only present for completeness, to ensure the agreement with non-linear simulations at smaller scales which does not participate much to the transport in mixing length models. This definition for the mixing length rule is modified by the linear eigenfunction shift $x_0$ proportional to the symmetry breakers (12). Indeed, the linear eigenfunction enters the expression of $\langle \theta^2 \rangle$ from (18):

$$\langle \theta^2 \rangle = \frac{\int \theta^2 \tilde{\phi} d\theta}{\int \tilde{\phi} d\theta} = \frac{2d^2}{\Re(\text{w}^2)}\frac{\Gamma(0.75)}{\Gamma(0.25)} + \frac{\Im(\text{x}_0)^2 d^2}{\Re(\text{w}^2)^2} \tag{19}$$

Therefore, the symmetry breakers influence $\langle k_\perp^2 \rangle$ through the imaginary part of the eigenfunction shift $\Im(\text{x}_0)$ and the real part of the mode width, the latter being proportional to the growth rate found in the fluid model. Thus, both $\gamma$ (see Sec. 4)
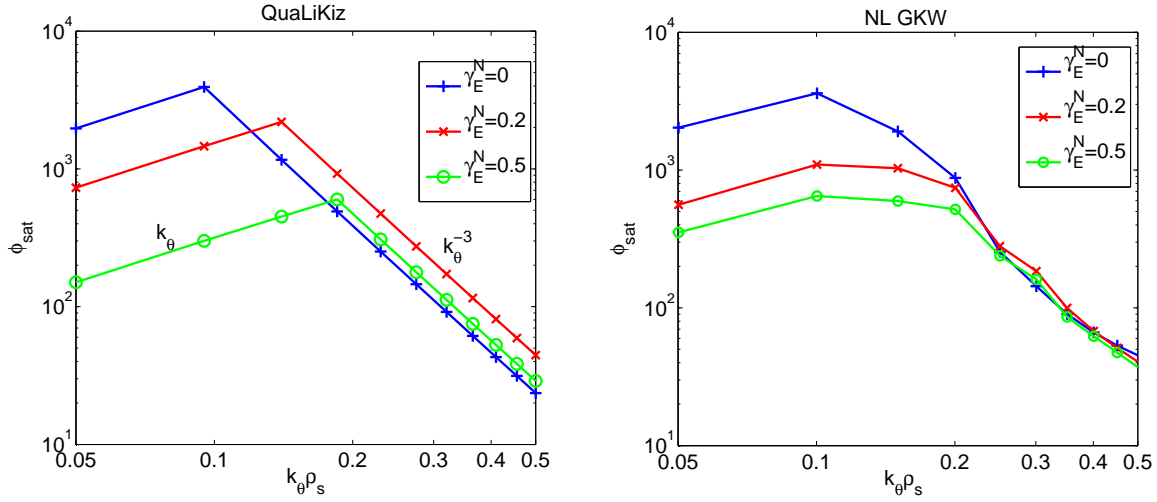
**Figure 8.** QuaLiKiz $\tilde{\phi}_{sat}$ estimate (left panel) and GKW non linear saturated potential. Simulations with $\mathbf{E} \times \mathbf{B}$ shear only. $\gamma_E$ values in $v_{Ti}/R$ units.

and $\langle k_\perp^2 \rangle$ are modified in the presence of finite sheared rotation. This approach is different than that of [22]. Indeed, since there is no parallel asymmetrization of the linear eigenmodes with the $\mathbf{E} \times \mathbf{B}$ shear in TGLF, a non-linear spectral shift model was built to compute the induced momentum flux. Here, the parallel asymmetrization of the linear eigenmodes with the $\mathbf{E} \times \mathbf{B}$ shear fulfills this task, avoiding using a non-linear spectral shift fitting model.

The modification of $\tilde{\phi}_{sat}$ induced by $\mathbf{E} \times \mathbf{B}$ shear are plotted and compared to non-linear GKW saturated potential [73] in Figure 8. In the simulations presented here, GA-std case parameter set has been employed with $u_\parallel = \nabla u_\parallel = 0$. Three values of $\mathbf{E} \times \mathbf{B}$ shear are chosen corresponding to an experimentally relevant range of $\gamma_E$ from 0 to $0.5R/v_{Ti}$. The $k_\theta \rho_s$ extent covered in Figure 8 corresponds to the transport relevant spectral range.

For both QuaLiKiz and GKW, as $\mathbf{E} \times \mathbf{B}$ shear is increased, the amplitude of the saturated potential is reduced at the largest scales (lowest wave numbers). In QuaLiKiz, this is due to a shift of the maximum of the saturated potential towards smaller scales corresponding to the usual picture of the non-linear effect of the $\mathbf{E} \times \mathbf{B}$ shear. In GKW, a flattening of the saturated potential amplitude is rather observed around its maximum. Both codes exhibit a weak dependence of their saturated potential with $\gamma_E$ at $k_\theta \rho_s > 0.2$. Quantitatively, in QuaLiKiz, the reduction of the saturated potential maximum amplitude is underestimated at lower $\mathbf{E} \times \mathbf{B}$ and overestimated at higher $\mathbf{E} \times \mathbf{B}$ shear values. Despite these quantitative differences, the non-linear fluxes quenching with $\mathbf{E} \times \mathbf{B}$ shear is captured qualitatively with a shifted eigenfunction calculated in the fluid limit. In the next section, the quasi linear fluxes are compared to non-linear simulations and the influence of the saturated potential of the fluxes is further discussed.
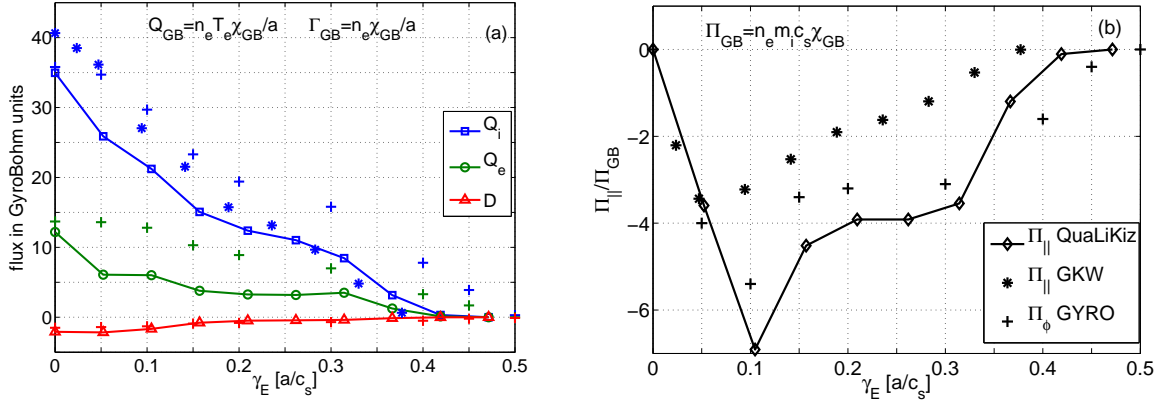
**Figure 9.** (a) Ion and electron heat fluxes, particle flux and (b) angular momentum flux for GA-std parameters. Here $\Pi_\parallel \equiv \Pi_{RS}$ since $u_\parallel = \nabla u_\parallel = 0$. The solid lines are QuaLiKiz results, the stars $*$ are GKW data from [73] and the crosses $+$ are GYRO data from [22]. $a/c_s$ units have to be multiplied by $3/\sqrt{2}$ to have their $R/v_{Ti}$ equivalent.

## 5.3. Comparison of QuaLiKiz fluxes with non-linear simulations

To finally evaluate the model presented above, the resulting heat, particle and momentum fluxes are compared to non linear simulations. First, the impact of $\mathbf{E} \times \mathbf{B}$ shear alone is studied in Figure 9, i.e. $u_\parallel$ and $\nabla u_\parallel$ are artificially set to 0. GA std case parameters are used to compare QuaLiKiz predictions with published results from non-linear GYRO [22] and GKW[73].

QuaLiKiz heat and particle fluxes are smoothly reduced and quenched for $\gamma_E > 0.4c_s/a$ as illustrated in Figure 9(a). This quench value is lower than what is found by GYRO simulations [see 22, Figure 1] but is in agreement with the value obtained with GKW [see 73, Table II] using non-linear GKW. QuaLiKiz predictions for the fluxes amplitude lies between non-linear GKW and non-linear GYRO for the ion heat flux. In GYRO the fluxes reduction with increasing $\mathbf{E} \times \mathbf{B}$ shear is notably slower than found with GKW and QuaLiKiz as illustrated by Figure 9(a).

The angular momentum flux $\Pi_\parallel$ is presented in Figure 9(b). As $u_\parallel$ and $\nabla u_\parallel$ are set to zero, $\Pi_\parallel$ corresponds to the residual stress $\Pi_{RS}$ in this case. In absolute value, the momentum flux increases at first with $\gamma_E$ due the $\mathbf{E} \times \mathbf{B}$ shear asymmetrization of the eigenfunction. Then, the momentum flux is slowly reduced due to the turbulence quenching by the $\mathbf{E} \times \mathbf{B}$ shear. This qualitative trend is in agreement with non-linear simulations. Quantitatively, QuaLiKiz overestimates the momentum flux found with GKW by $\sim 50\%$ but is in agreement with GYRO simulations. GYRO was run with a circular Miller equilibrium retaining the finite $\epsilon$ effects, which are not present in the GKW simulations with the $\hat{s} - \alpha$ equilibrium nor in QuaLiKiz. The discrepancy between QuaLiKiz and GKW is related to the overestimation of the saturated potential amplitude at lower $k_\theta \rho_s$ and intermediate values of $\gamma_E$ in QuaLiKiz detailed in the previous section. This is a necessary trade-off to estimate the $\mathbf{E} \times \mathbf{B}$ shear induced turbulence quench and

momentum flux in a reduced model compatible with the integrated modeling framework without using any fitting model. It is interesting to note that a fluid model captures the essential physical mechanisms of the complex $\mathbf{E} \times \mathbf{B}$ shear action on the modes.

Now, the effect of $\nabla u_\parallel$ and $u_\parallel$ on the momentum flux are analyzed. To perform this analysis, the following non dimensional quantities are employed: The Prandtl number $\frac{\chi_\parallel}{\chi_i}$ and the pinch number $\frac{RV_\parallel}{\chi_\parallel}$. They facilitate the comparison with non linear simulations as the saturated potential does not appear in these ratio.

In QuaLiKiz, isolating conductive and convective contributions to the momentum flux is not straightforward due to $x_0$ dependencies presented in Sec. 5.1. To evaluate the different parts of the momentum flux, the 3-point presented in Sec. 5.1 can be simplified when dealing with test cases. A simulation with only $\nabla u_\parallel$ as a symmetry breaker ($u_\parallel = \gamma_E = 0$) is performed. The ratio of the momentum flux to the ion heat flux then gives the Prandtl number. To evaluate the *total* convective part, a simulation with only $u_\parallel - \nabla u_\parallel = \gamma_E = 0$ – is carried out. The ratio between the resulting momentum flux to the previous $\nabla u_\parallel$-only momentum flux gives the pinch number. In the following, this method is called *2-point method*. Compared to the 3-point method, the modification of the conductivity by $\mathbf{E} \times \mathbf{B}$ shearing (through the force balance equation) is neglected. Indeed, $\gamma_E$ is artificially put to 0 as is usually done in momentum diffusivity/pinch analysis with non-linear gyro-kinetic simulations [30].

Two QuaLiKiz simulations based on GA-std case parameter set are performed for the validation of the conductive and convective contributions to the momentum flux calculated by the 2-point method:

- one with $\frac{-R\nabla u_\parallel}{v_{Ti}} = 1$, $\frac{u_\parallel}{v_{Ti}} = 0$;
- one with $\frac{-R\nabla u_\parallel}{v_{Ti}} = 0$, $\frac{u_\parallel}{v_{Ti}} = 0.2$.

As explained in Sec. 5.1, a direct extraction of a $\Pi_{\nabla u}$ and a $\Pi_u$ – corresponding to diffusive and convective contributions to the momentum transport *without* taking the eigenfunction shift effect into account – is possible in QuaLiKiz. This method called *direct separation method* is compared to the 2-point method in Figure 10 to give an idea of the impact of the eigenfunction shift on $\chi_\parallel$ and $V_\parallel$.

The normalized density gradient $R/L_n$ was varied from 0 to 4. Indeed, results from non-linear gyrokinetic simulations indicate a strong correlation between $R/L_n$ and the pinch number [30, 65], the Prandtl number being weakly correlated. In Figure 10, the Prandtl number is displayed with crosses and the pinch number with circles, the results from the 2-point method being in plain curves and the estimations via direct separation in dashed curves.

The Prandtl number deduced from the 2-point method is found to be close to 0.7 agreeing with quasi-linear [19] and non-linear simulations[30]. Due to the omission of the eigenfunction shift effect, the direct separation in QuaLiKiz gives a higher Prandtl number, close to one, as predicted in early theoretical calculations[61]. Using the 2-point method, the pinch number $\frac{RV_\parallel}{\chi_\parallel}$ is found to vary from $-2$ to $-5$, with a strong correlation with $R/L_n$, as in [30]. When neglecting the eigenfunction shift effects, i.e.
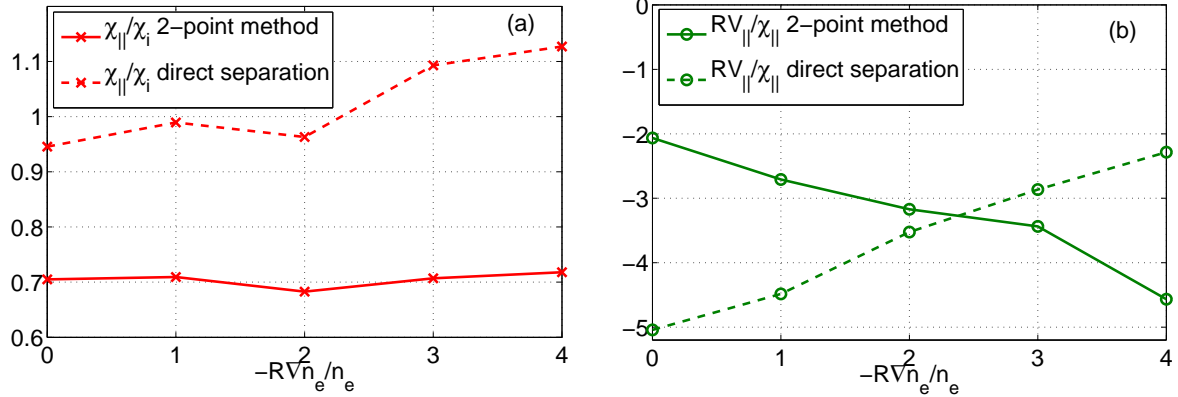
**Figure 10.** (a) Prandtl (red crosses) and (b) pinch number (green circles) calculated with the *direct separation method* (dashed curves) and with the *2-point method*[30] (plain curves)

with the direct separation technique, the correlation with $R/L_n$ is inverted. Taking the ratio of the momentum fluxes amplifies the error. This illustrates that the eigenfunction shift has to be taken into account to have the correct dependencies and values of the momentum flux.

To summarize this section, the quasi-linear momentum flux derived in Sec. 5.1 was successfully benchmarked against non-linear simulations, including the momentum diffusivity, the momentum pinch and the residual stress. For the conductive and convective parts of the momentum flux, two methods were presented and compared. The importance of the eigenfunction shift contribution was illustrated. In the next section, the influence of the $\mathbf{E} \times \mathbf{B}$ shear on the momentum flux will be analyzed with QuaLiKiz and compared to the experimental results.

## 6. Comparison with the experiment

In this final section, a JET H-mode shot is analyzed with QuaLiKiz. The Prandtl and pinch numbers are found compatible with the experiment on a large part of the radius. However the effective ion heat flux is significantly compared to the experimental value from JETTO in interpretative mode.

The analyzed shot, from Tala et al.[4], is an NBI modulation experiment proving the experimental evidence of a momentum pinch. To evidence the presence of a momentum pinch, the amplitude and phase of the modulated toroidal velocity was simulated with JETTO:

- either with only momentum diffusivity *i.e.* $\chi_\phi/\chi_i = \chi_{\phi,\text{eff}}/\chi_i \approx 0.25$
- or with both momentum diffusivity and pinch. $\chi_\phi/\chi_i = 1$ matching theory based estimations [61] in older calculations[41], or computed with gyrokinetic simulations [4], and $v_{pinch} \approx 15\text{m/s}$ adapted to match the experimental effective diffusivity $\chi_{\phi,\text{eff}}$ or, equivalently, the modulated toroidal velocity amplitude.
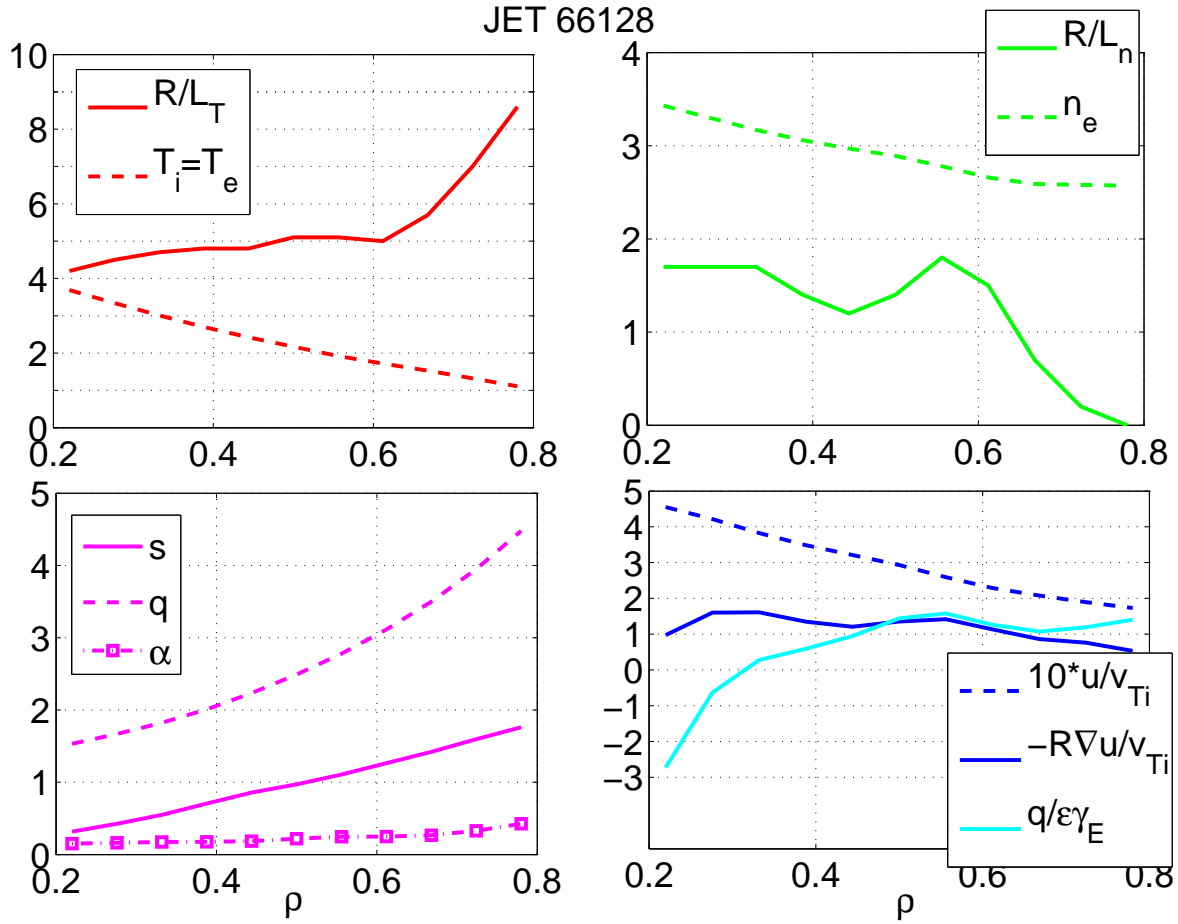
**Figure 11.** Input parameters for QuaLiKiz simulation of JET shot 66128. All parameters were taken from JETTO fit realized for GKW simulations of [4] except $T_i = T_e$. $Z_{eff} = 2$

Tala et al.[4, 41] showed that both the amplitude and the phase of the experimental toroidal velocity are only correctly reproduced when a momentum pinch is taken into account. However, the residual stress was neglected in their analysis. Quasi-linear gyrokinetic simulations are performed with QuaLiKiz. The global parameters are the ones used in GKW for Figure 3 of [4]. The main input parameters of the simulation are displayed in Figure 11. All parameters are taken from JETTO interpretative run performed for GKW simulation of [4] with the exception of $T_i = T_e$ as there is no evidence from the CX and ECE signals for $T_i \neq T_e$. Since QuaLiKiz has a circular equilibrium the gradients are averaged over the flux surface.

The $\mathbf{E} \times \mathbf{B}$ shear calculated with the radial force balance equation on the carbon impurity is significant in this shot, as indicated in Figure 11. Since the collisionality is weak in this shot — $\nu^* \in [0.03; 0.08]$ — the neoclassical value for the poloidal velocity is given by the banana regime value $v_{\theta,C} B_\varphi = 1.17 \nabla T_C / 6e$. The *3-point method* presented in Sec. 5.1 is used to correctly account for the different contributions to the momentum flux and quantify the momentum diffusivity, the momentum pinch and the
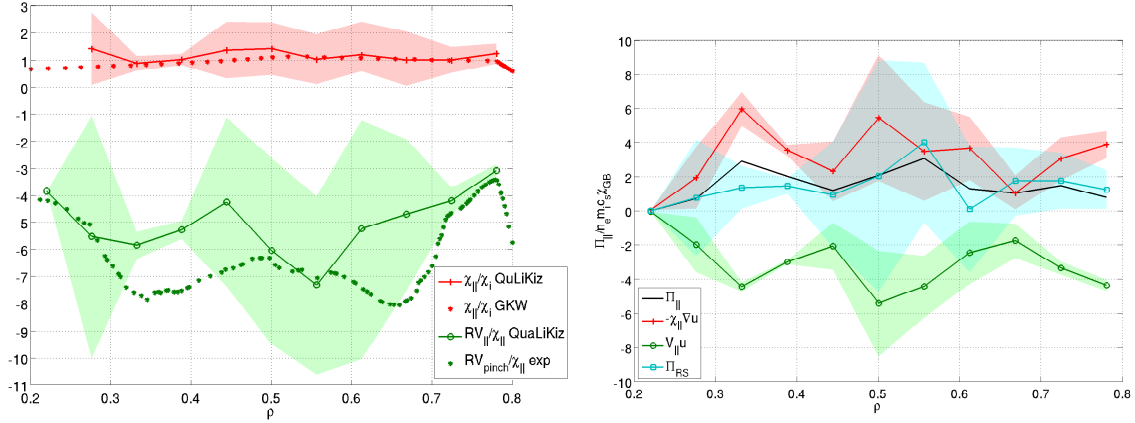
**Figure 12.** Left: Prandtl number (red crossed) and pinch number(green circles) calculated by a 3-point method. Right: Detail of the different contributions to $\Pi_\parallel$.

residual stress. As indicated in Sec. 5.1, a simulation is performed with the experimental conditions described in Figure 11, one is performed with the parallel velocity modified by $\pm 20\%$ with the corresponding modification in $\gamma_E$ and $\nabla u_\parallel$ and one with the parallel velocity *incremented* by $\pm 0.05 V_{Ti}/R$ with the corresponding modification of $\gamma_E$ but no change in $\nabla u_\parallel$. The resulting Prandtl and pinch numbers are given in Figure 12(a). The colored regions in this plot corresponds to the uncertainties linked to the linearization performed to extract these numbers. They are calculated by performing 5 simulations with different modifications of the velocity and combining the results.

The estimated Prandtl number lies within 0.8 and 1.4, close to GKW predictions used in [4]. The pinch number calculated with QuaLiKiz ranges from 3 to 7, in good agreement with the experimental values ranging from 3 to 8. The large uncertainties obtained with the 3-point method indicates that the momentum flux changes in a complex way with $u_\parallel$ and $\nabla u_\parallel$ which the linearization employed to get Figure 12(a) does not reflect.

The contributions to the momentum flux from $u_\parallel$, $\nabla u_\parallel$ and the residual stress are compared in Figure 12(b). The estimated residual stress seems not entirely negligible in this shot. However a definitive conclusion would require smaller error bars. Moreover some significant contributions to the residual stress are not taken into account in local models such as QuaLiKiz as pointed out by [37].

Finally ,the pinch velocity itself $-V_\parallel$ (plain curve) is plotted along with the effective ion heat flux $\chi_{i,eff}$ (dashed curve) in Figure 13 and compared to the experimental estimates. To improve the robustness of the results and reproduce experimental uncertainties, $R/L_T$ was varied by 20% with the associated modification of $\gamma_E$. It corresponds to the colored regions of Figure 13. Even when increasing the temperature gradients by 20% $\chi_{i,eff}$ is underestimated compared to the experiment. This advocates for including a more refined magnetic equilibrium in QuaLiKiz. Indeed, averaging over the flux surface is a way to take the stabilizing effect of the elongation into account. However, it appears that the stabilization is overestimated by this method. Increasing
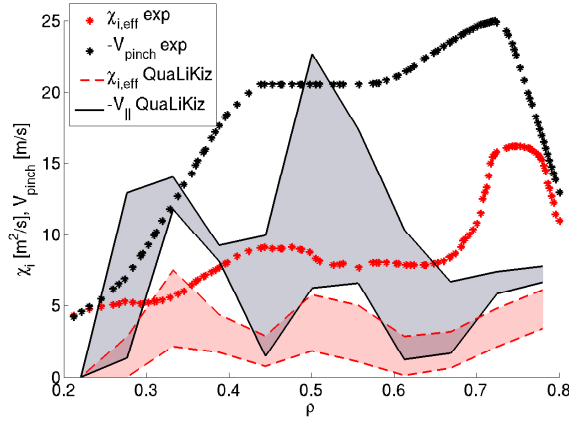
**Figure 13.** Ion heat flux diffusivity (red dashed) and pinch velocity (plain). The colored regions correspond to a 20% variation of $R/L_T$ with associated variation of $\gamma_E$.

by 20% the gradients gives a closer results. This is equivalent to taken the gradient at the midplane. According to the good agreement on the pinch and the Prandtl number, $V_\parallel$ is also underestimated in QuaLiKiz. Outside $\rho = 0.5$, the discrepancy between QuaLiKiz and JETTO predictions enlarges. This may comes from the choice of $T_e = T_i$ made in QuaLiKiz simulations based on CX and ECE signals in disagreement with JETTO fit. However, the fact that JETTO runs fail to reproduce the experimental phase of the modulated velocity at this radii is worth noticing.

To summarize, considering the experimental uncertainties on the various gradients used as inputs, QuaLiKiz estimations of the Prandtl number and the momentum pinch are close enough to the ones evaluated from the experiment. In particular, an inward convective flux of momentum is found in the model and the experiment with a pinch number ranging from 5 to 8. However, a quantitative analysis on the fluxes intensity remains difficult due to the fluxes sensitivity to the temperature gradients combined with the difficulty to measure them accurately in experiments. To overcome this issue, the present version of QuaLiKiz has to be coupled to an integrated platform such as CRONOS. This will enable driving QuaLiKiz via the sources which is more relevant physically than to impose the gradients.

## 7. Conclusions

With the aim to improve and broaden the capabilities of first principle based transport models for integrated modeling, the gyrokinetic transport code QuaLiKiz[2, 3, 58] has been upgraded to include sheared flow effects and momentum flux calculation.

For momentum studies, the shape of the eigenfunctions in the parallel direction is essential as illustrated in section 5.3. The reduced fluid model used for QuaLiKiz eigenfunctions was shown to recover the correct dependencies with the parallel velocity, its gradient and the $\mathbf{E} \times \mathbf{B}$ shear without any "free-fitting parameters" even close

to the turbulent threshold; by direct comparisons with self-consistent gyrokinetic eigenfunctions for $u_\parallel$ and $\nabla u_\parallel$. Recovering the low-$k$ turbulence quench, the heat and particle fluxes reduction and the residual stress induced by $\mathbf{E} \times \mathbf{B}$ shear from non-linear simulations demonstrated that $\mathbf{E} \times \mathbf{B}$ shear modeling is valid as well. The results on the residual stress remarkably showed that a shift of the linear eigenfunctions is enough to get the correct effect of the $\mathbf{E} \times \mathbf{B}$ shear on the saturated potential with a mixing length rule.

Separating the different contributions from $u_\parallel$, $\nabla u_\parallel$ and $\mathbf{E} \times \mathbf{B}$ shear to the momentum flux appeared to be challenging. With a *3-point method*, the momentum diffusivity and pinch and the $\mathbf{E} \times \mathbf{B}$ induced residual stress can be calculated. The Prandtl and pinch numbers calculated this way showed good agreement with both non-linear simulations and NBI modulation experimental results. In particular, the correlation of the pinch number with $R/L_n$ was recovered. The residual stress was evaluated but no definitive conclusions should be drawn due to the uncertainties linked to the 3-point method i.e. the total flux is not linear in $u_\parallel$, $\nabla u_\parallel$, $\gamma_E$. The insight gained by analyzing experiments dedicated to the residual stress characterization appears limited in the local approach taken in QuaLiKiz. Since the residual stress is a higher $\rho^*$ quantity, it cannot be properly determined by local simulations.

From NBI modulation experiments, the variability of QuaLiKiz predictions within experimental uncertainties was underlined, pointing out the limitations of gradient driven simulations for comparisons with experiments.

Finally, with the new features presented in this paper, QuaLiKiz opens the way for simulating consistently $T_e$, $T_i$, $n_e$ and $v_\parallel$ profiles in integrated modeling platforms such as CRONOS. This will have the side benefit of driving QuaLiKiz with the sources instead of imposing the gradients, improving its prediction capabilities.

## Acknowledgments

## Appendix A. Passing particle functional

Before integration the passing particle functional reads:

$$
\mathcal{I}_{s,pass} = \sum_{\epsilon_\parallel = \pm 1} \frac{\left(1 + \frac{2u_\parallel}{v_{Ts}}\epsilon_\parallel\sqrt{\xi(1-\lambda b)} + \frac{u_\parallel^2}{v_{Ts}^2}\left(2\xi(1-\lambda b)-1\right)\right)}{}
$$

$$
\frac{\frac{R}{L_{Ts}}^*\xi + 2\left(\frac{R}{L_u} - \frac{R}{L_{Ts}}\right)\frac{u_\parallel}{v_{Ts}}\epsilon_\parallel\sqrt{\xi(1-\lambda b)} + \frac{R}{L_{ns}} - \frac{3}{2}\frac{R}{L_{Ts}} + \frac{u_\parallel^2}{v_{Ts}^2}\left(\frac{R}{L_{Ts}} - 2\frac{R}{L_u}\right) - \frac{\varpi}{n\bar\omega_{ds}}}{(2-\lambda b)f_\theta\xi + \epsilon_\parallel\frac{x}{d}\frac{\omega_b}{n\bar\omega_{ds}} - \frac{\varpi}{n\bar\omega_{ds}} + \imath 0^+}
$$

$$
(A.1)
$$

The integration over $\lambda$ and $\xi$ is then performed. In QuaLiKiz, the integration over $\lambda$, not tractable analytically, is simplified. It is considered that the passing particle pitch-angle variation does not influence the drift frequencies so that they can be averaged over $\lambda$. This assumption is correct for the curvature and $\nabla B$ drift for which the pitch angle variation represents no more than 50% of its value. For $k_\parallel v_\parallel$ expression however, this means that its value will be overestimated for barely passing particles. The result is given in ( A.2) using the Fried-Conte function $Z(z) = \frac{1}{\sqrt\pi}\int_{-\infty}^{+\infty}\frac{e^{-v^2}}{v-z}dv$.

$$
\langle\mathcal{I}_{s,pass}\rangle_p = \frac{3f_p}{2f_\theta}\left[\frac{R}{L_{Ts}}\frac{Z_2(V_+) - Z_2(V_-)}{V_+ - V_-} + \left(\frac{R}{L_{ns}} - \frac{3}{2}\frac{R}{L_{Ts}} - \frac{\varpi}{n\bar\omega_{ds}}\right)\frac{Z_1(V_+) - Z_1(V_-)}{V_+ - V_-}\right]
$$
$$
+ \frac{3f_p}{f_\theta}\left[\frac{u_\parallel}{v_{Ts}}\frac{R}{L_{Ts}}\frac{V_+ Z_2(V_+) - V_- Z_2(V_-)}{V_+ - V_-} + \left(\frac{R}{L_u} + \frac{u_\parallel}{v_{Ts}}\left(\frac{R}{L_{ns}} - \frac{5}{2}\frac{R}{L_{Ts}} - \frac{\varpi}{n\bar\omega_{ds}}\right)\right)\frac{V_+ Z_1(V_+) - V_- Z_1}{V_+ - V_-}\right.
$$
$$
+ \frac{f_p}{f_\theta}\frac{u_\parallel}{v_{Ts}}\left[A_T\frac{u_\parallel}{v_{Ts}}\frac{Z_3(V_+) - Z_3(V_-)}{V_+ - V_-} + \left(2\frac{R}{L_u}\frac{u_\parallel}{v_{Ts}}\left(\frac{R}{L_{ns}} - \frac{7}{2}\frac{R}{L_{Ts}} - \frac{\varpi}{n\bar\omega_{ds}}\right)\right)\frac{Z_2(V_+) - Z_2(V_-)}{V_+ - V_-}\right]
$$
$$
- \frac{3f_p}{f_\theta}\frac{u_\parallel}{v_{Ts}}\left[\frac{R}{L_{Ts}}\frac{u_\parallel}{v_{Ts}}\frac{Z_2(V_+) - Z_2(V_-)}{V_+ - V_-} + \left(2\frac{R}{L_u}\frac{u_\parallel}{v_{Ts}}\left(\frac{R}{L_{ns}} - \frac{5}{2}\frac{R}{L_{Ts}} - \frac{\varpi}{n\bar\omega_{ds}}\right)\right)\frac{Z_1(V_+) - Z_1(V_-)}{V_+ - V_-}\right]
$$

$$
(A.2)
$$

where $f_p$ is the passing particle fraction. $Z_1$, $Z_2$ and $Z_3$ are defined are based on the Fried-Conte function $Z$: $Z_1(z) = z + z^2 Z(z)$, $Z_2(z) = \frac{1}{2}z + z^2 Z_1(z)$ and $Z_3(z) = \frac{3}{4}z + z^2 Z_2(z)$. The variables $V_+$ and $V_-$ correspond to the poles of (A.1). They are defined by:

$$
V_\pm = \frac{1}{2}\frac{v_{Ts}x}{qRd}\frac{\bar\omega_b}{f_\theta n\bar\omega_{ds}} \pm \sqrt\Delta
$$
$$
\Delta = \left(\frac{1}{2}\frac{v_{Ts}x}{qRd}\frac{\bar\omega_b}{f_\theta n\bar\omega_{ds}}\right)^2 + \frac{\varpi}{f_\theta n\bar\omega_{ds}}
$$

$$
(A.3)
$$

The integration over $k_r$ remains to be performed. As expressed in (5), there remain some $x$ dependence in the passing particle functional. Moreover, $\varpi = \omega - n\omega_{E\times B}$ contains an $x$ dependence too. To take all effects into account, an integration over $k_r$ and $x = r - r_0$, where $x \ll r_0$, is performed as derived by Garbet et al.[42]

and presented first in App. A.4.2 of [1] for QuaLiKiz framework. The expression of $\mathcal{L}_{s,pas.} = \int_{-\infty}^{+\infty} \frac{dk_r}{2\pi} \langle \mathcal{I}_{s,pass} \rangle_p \mathcal{B}_0(k_\theta \rho_s)$ is then transformed into:

$$\mathcal{L}_{s,pas.} = \int_{-\infty}^{\infty} \frac{dk_+}{2\pi} \iint_{-\infty}^{\infty} dx_+ dx_- \tilde{\phi}(x_+ - \frac{x_-}{2}) \tilde{\phi}^*(x_+ + \frac{x_-}{2}) e^{\imath k_+ x_-} \langle \mathcal{I}_{s,pass} \rangle_p \mathcal{B}_0(k_\theta \rho_s) \quad (A.4)$$

As shown in section 3 – in presence of $u_\parallel$, $\nabla u_\parallel$ and $\mathbf{E} \times \mathbf{B}$ shear – $\tilde{\phi}(x)$ is a shifted Gaussian:

$$\tilde{\phi}(x) = \phi_0 \exp(-\frac{(x - x_0)^2}{2w^2}) \quad (A.5)$$

Therefore, the product $\phi\phi^*$ can be written as:

$$\tilde{\phi}\tilde{\phi}^* = \phi_0^2 \exp\left( -\frac{(x_+ - \Re(x_0) - k_+ \Im(w^2))^2}{\Re(w^2)} - \Re(w^2)\left(k_+ - \frac{\Im(x_0)}{\Re(w^2)}\right)^2 \right) \quad (A.6)$$

Dimensionless quantities $\rho^*$ and $k^*$ are defined for the integration over $x_+$ and $k_+$:

$$\rho^{*2} = \frac{(x_+ - \Re(x_0) - k_+ \Im(w^2))^2}{\Re(w^2)}$$
$$k^{*2} = \Re(w^2)\left(k_+ - \frac{\Im(x_0)}{\Re(w^2)}\right)^2 \quad (A.7)$$

In (A.3), $x$ is replaced by $\rho^* \sqrt{\Re(w^2)} + \Re(x_0) + k\Im(w^2)$ and $k = \frac{k^*}{\sqrt{\Re(w^2)}} + \frac{\Im(w^2)}{\Re(w^2)}$, $\Re(w^2)$ being defined positive which ensures $\left|\tilde{\phi}\right|^2$ is finite. The passing particle functional then become:

$$\mathcal{L}_{s,pass} = \int_{-\infty}^{\infty} \frac{dk^*}{\sqrt{\pi}} e^{-k^{*2}} \int_{-\infty}^{\infty} \frac{d\rho^*}{\sqrt{\pi}} e^{-\rho^{*2}} \langle \mathcal{I}_{s,pass} \rangle_p (k^*, \rho^*) \mathcal{B}_0(k_\theta \rho_s) \quad (A.8)$$

## Appendix B. Trapped particle functionals

For trapped particles, there are no $\theta$ dependence in the drifts, since the bounce average is performed. $k_\parallel v_\parallel$ is therefore expressed in terms of the poloidal wave number $m$:

$$k_\parallel v_\parallel = \pm \frac{m v_{Ts}}{qR} \sqrt{\xi(1 - \lambda b)} \quad (B.1)$$

It is also stressed that no assumption is taken on $\lambda$.

$$\mathcal{I}_{i,m,tr} = \sum_{\epsilon_\parallel = \pm 1} \left( 1 + \frac{2u_\parallel}{v_{Ts}} \epsilon_\parallel \sqrt{\xi(1 - \lambda b)} + \frac{u_\parallel^2}{v_{Ts}^2} (2\xi(1 - \lambda b) - 1) \right)$$
$$\frac{\frac{R}{L_{Ts}}^* \xi + 2(\frac{R}{L_u} - \frac{R}{L_{Ts}}) \frac{u_\parallel}{v_{Ts}} \epsilon_\parallel \sqrt{\xi(1 - \lambda b)} + \frac{R}{L_{ns}} - \frac{3}{2} \frac{R}{L_{Ts}} + \frac{u_\parallel^2}{v_{Ts}^2}(\frac{R}{L_{Ts}} - 2\frac{R}{L_u}) - \frac{\varpi}{n\bar{\omega}_{ds}}}{(2 - \lambda b) f_\theta \xi + \epsilon_\parallel m \frac{\omega_b}{n\bar{\omega}_{ds}} - \frac{\varpi}{n\bar{\omega}_{ds}} + \imath 0^+}$$
$$(B.2)$$

The attentive reader noticed that (B.2) is expressed for trapped ions. Its expression is different for trapped electrons because electron-ion collisions are integrated in QuaLiKiz. Since the effect of collisionality is most important on trapped electrons[84], collisions are only implemented in trapped electron functionals as detailed in [34]. For $\mathcal{I}_{e,m,tr}$, $\nu_{ie}$ is included in (B.2) in place of the Landau prescription for causality, the small quantity $\imath o^+$, through a Krook operator presented in [34]. The expression of $\mathcal{I}_{e,m,tr}$ is

$$
\mathcal{I}_{e,m,tr} = \sum_{\epsilon_\parallel = \pm 1} \left( 1 + \frac{2u_\parallel}{v_{Ts}} \epsilon_\parallel \sqrt{\xi(1-\lambda b)} + \frac{u_\parallel^2}{v_{Ts}^2} \left(2\xi(1-\lambda b) - 1\right) \right)
$$

$$
\frac{\frac{R}{L_{Ts}}^*\xi + 2(\frac{R}{L_u} - \frac{R}{L_{Ts}})\frac{u_\parallel}{v_{Ts}}\epsilon_\parallel\sqrt{\xi(1-\lambda b)} + \frac{R}{L_{ns}} - \frac{3}{2}\frac{R}{L_{Ts}} + \frac{u_\parallel^2}{v_{Ts}^2}(\frac{R}{L_{Ts}} - 2\frac{R}{L_u}) - \frac{\varpi}{n\bar{\omega}_{ds}}}{(2-\lambda b)f_\theta\xi + \epsilon_\parallel m\frac{\omega_b}{n\bar{\omega}_{ds}} - \frac{\varpi}{n\bar{\omega}_{ds}} + \imath\frac{\nu_{fe}(\xi,\lambda)}{n\bar{\omega}_{ds}}}
$$

(B.3)

where $\nu_{fe} = \nu_{ei}\left(\frac{v_{Te}}{\sqrt{\xi}}\right)^3 Z_{\text{eff}}\left(\frac{\epsilon}{|1-\epsilon-\lambda|^2}\frac{0.111\delta + 1.31}{11.79\delta + 1}\right)$ with $\delta = \left(\frac{|\omega|}{37.2/\epsilon Z_{\text{eff}}\nu_{ei}}\right)^{1/3}$ [34].

Now, before performing the integral over $(\xi, \lambda)$, it is worth noticing that $\mathcal{B}_1$ is odd in $k_r$. When integrating over $k_r$, it will only give a non-zero value for $\langle \mathcal{I}_{s,1,tr} \rangle$ in presence of an asymmetric eigenfunction in $k_r$. This happens only in the presence of a parallel velocity symmetry breaker[19]: $u_\parallel$, $\nabla u_\parallel$ or $\mathbf{E} \times \mathbf{B}$ shear in QuaLiKiz framework. Given the fact that the Krook operator does not conserve momentum, it appears inadequate to keep this higher order term in the equation. Since $\mathcal{B}_2$ represents 5% of $\mathcal{B}_0$ when integrated over $k_r$, higher order are not treated neither. This is why the only term actually used in QuaLiKiz is $m = 0$. (B.4) therefore expresses the trapped ions functional integrated over $(\xi, \lambda)$.

$$
\langle \mathcal{I}_{0,i,tr} \rangle_t = 2f_t \int_0^1 \frac{K(\kappa)\kappa}{f(\kappa)} d\kappa \left[ \left(1 - \frac{u_\parallel^2}{v_{Ti}^2}\right)\left(\frac{R}{L_{Ti}}\frac{Z_2(z)}{z} + \left(\frac{R}{L_{ni}} - \frac{3}{2}\frac{R}{L_{Ti}} - z^2\right)\frac{Z_1(z)}{z}\right) \right.
$$

$$
\left. - \frac{u_\parallel}{v_{Ti}}\left(2\frac{R}{L_u} - \frac{u_\parallel}{v_{Ti}}\frac{R}{L_{Ti}}\right) \right]
$$

(B.4)

where $z$ is the square root of $\frac{\varpi}{n\bar{\omega}_{ds}}$ which has a positive imaginary part and $f_\kappa = 2\frac{E(\kappa)}{K(\kappa)} - 1 + 4s\left(\kappa^2 - 1 + \frac{E(\kappa)}{K(\kappa)}\right) = \oint \frac{d\theta}{2\pi}\frac{f_\theta}{4\sqrt{1-\lambda b}}$ with $\lambda = 1 - 2\epsilon\kappa^2$. Comparing (B.4) to (A.2), the reader might have noticed that the second and third terms (lines) of (A.2) are absent in (B.4). Indeed, the integration over $\lambda$ gives $1 - 2\epsilon$ for passing particles and $2\epsilon$ for trapped ions for the second term and $\frac{1}{3}$ for passing and $\frac{2}{3}f_t\epsilon$ for trapped ions for the third term. So, at lowest order in $\epsilon$, the expression for the trapped ions functional $\langle \mathcal{I}_{0,tr} \rangle$ comes down to (B.4). For trapped electrons, the expression (B.3) is numerically integrated over $(\xi, \kappa)$.

The integration over $k_r$ is simplified by bounce averaging. Integration over $\theta$ being already performed for $\mathcal{I}_{0,tr}$ by bounce averaging, the only $k_r$ dependence in $\mathcal{L}_{s,tr}$ lies in

$\mathcal{B}_0(k_r\delta_s)|\tilde{\phi}_{n\omega}|^2$ which is integrated in $k_r$ numerically. The Bessel function $\mathcal{B}_0(k_r)$ is not included in the integration above because $\rho_s \ll \delta_s$). The expression for the trapped particle functionals: $\mathcal{L}_{0,s,tr}$ can then be written

$$\mathcal{L}_{0,s,tr} = \int_0^1 K(\kappa)\kappa\mathcal{I}_{0,tr}\mathrm{d}\kappa\mathcal{B}_0(k_\theta\rho_s)\int\frac{\mathrm{d}k_r}{2\pi}\mathcal{B}_0(k_r\delta_s)|\tilde{\phi}_{n\omega}(k_r)|^2 \tag{B.5}$$

## Appendix C. Quasi-linear momentum flux derivation

Using the formalism developed in Sec. 2 and the notations from the former appendices, the complete expression of $\Pi_\parallel$ is:

$$\Pi_\parallel = -\sum_{\epsilon_\parallel=\pm1,s,n}\frac{n_sm_s}{B}\left(\frac{nq}{r}\right)^2\left\langle \epsilon_\parallel\xi v_{Ts}\sqrt{1-\lambda b}e^{-\xi}\left(1+2\frac{u_\parallel}{v_{Ts}}\epsilon_\parallel\sqrt{\xi(1-\lambda b)}+\frac{u_\parallel}{v_{Ts}}^2(2\xi(1-\lambda b)-1)\right)\right.$$
$$\left[\frac{R\nabla n_s}{n_s}+\left(\xi-\frac{u_\parallel}{v_{Ts}}\left(2\epsilon_\parallel\sqrt{\xi(1-\lambda b)}-\frac{u_\parallel}{v_{Ts}}\right)-\frac{3}{2}\right)\frac{R\nabla T_s}{T_s}+\right.$$
$$\left.2\left(\epsilon_\parallel\sqrt{\xi(1-\lambda b)}-\frac{u_\parallel}{v_{Ts}}\right)\frac{R\nabla u_\parallel}{v_{Ts}}+\frac{\varpi}{n\omega_{ds}}\right]\Im\left(\frac{1}{\omega-n\Omega_J(\xi,\lambda)+\imath0^+}\right)\left|\tilde{\phi}_{n\omega}\right|^2\right\rangle_{\xi,\lambda,k_r} \tag{C.1}$$

Apart from the saturated potential $\tilde{\phi}_{n\omega}$, the rest of the expression is similar to the linear gyrokinetic response presented in Sec. 2 except that only the imaginary part is of interest for the flux and that the integrations over $(\xi,\lambda)$ are slightly different due to the multiplication by $v_\parallel = \pm v_{Ts}\sqrt{\xi(1-\lambda b)}$. The same techniques as before are then employed. The contributions from trapped and passing particles to the momentum flux are treated separately.

$$\Pi_\parallel = -\sum_{\epsilon_\parallel=\pm1,s,n}\frac{n_sm_sv_{Ts}}{B}\left(\frac{nq}{r}\right)^2\left\{\int_{-\infty}^\infty\frac{\mathrm{d}k^*}{\sqrt{\pi}}e^{-k^{*2}}\int_{-\infty}^\infty\frac{\mathrm{d}\rho^*}{\sqrt{\pi}}e^{-\rho^{*2}}\Im(\mathcal{J}_{s,pass}(k^*,\rho^*))\mathcal{B}_0(k_\theta\rho_s)\left|\tilde{\phi}_n\right|^2\right.$$
$$\left.+\Im(\mathcal{J}_{s,tr})\int\frac{\mathrm{d}k_r}{2\pi}\mathcal{B}_0(k_\theta\rho_s)\mathcal{B}_0(k_r\delta_s)\left|\tilde{\phi}_n(k_r)\right|^2\right\} \tag{C.2}$$

The expression for $\mathcal{J}_{s,pass}$ is detailed in (C.3). Its expression is very close to that of A.1. A notable difference is that even functions ($Z1$, $Z2$, $Z3$) are replaced by odd functions

$(vZ1(v), vZ2(v), vZ3(v))$. This indicates that without rotation the momentum is zero.

$$
\begin{aligned}
\mathcal{J}_{s,pass} = \frac{2}{f_\theta} &\left[ \frac{R}{L_{Ts}} \frac{V_+ Z_2(V_+) - V_- Z_2(V_-)}{V_+ - V_-} + \left( \frac{R}{L_{ns}} - \frac{3}{2} \frac{R}{L_{Ts}} - \frac{\varpi}{n\bar{\omega}_{ds}} \right) \frac{V_+ Z_1(V_+) - V_- Z_1(V_-)}{V_+ - V_-} \right] \\
+ \frac{4}{3f_\theta} &\left[ \frac{u_\parallel}{v_{Ts}} \frac{R}{L_{Ts}} \frac{Z_3(V_+) - Z_3(V_-)}{V_+ - V_-} + \left( \frac{R}{L_u} + \frac{u_\parallel}{v_{Ts}} \left( \frac{R}{L_{ns}} - \frac{5}{2} \frac{R}{L_{Ts}} - \frac{\varpi}{n\bar{\omega}_{ds}} \right) \right) \frac{Z_2(V_+) - Z_2(V_-)}{V_+ - V_-} \right] \\
+ \frac{u_\parallel}{f_\theta v_{Ts}} &\left[ \frac{u_\parallel}{v_{Ts}} \frac{R}{L_{Ts}} \frac{V_+ Z_3(V_+) - V_- Z_3(V_-)}{V_+ - V_-} + \left( 2\frac{R}{L_u} + \frac{u_\parallel}{v_{Ts}} \left( \frac{R}{L_{ns}} - \frac{7}{2} \frac{R}{L_{Ts}} - \frac{\varpi}{n\bar{\omega}_{ds}} \right) \right) \frac{V_+ Z_2(V_+) - V_- Z_2(V_-)}{V_+ - V_-} \right] \\
- \frac{2u_\parallel}{f_\theta v_{Ts})} &\left[ \frac{u_\parallel}{v_{Ts}} \frac{R}{L_{Ts}} \frac{V_+ Z_2(V_+) - V_- Z_2(V_-)}{V_+ - V_-} + \left( 2\frac{R}{L_u} + \frac{u_\parallel}{v_{Ts}} \left( \frac{R}{L_{ns}} - \frac{5}{2} \frac{R}{L_{Ts}} - \frac{\varpi}{n\bar{\omega}_{ds}} \right) \right) \frac{V_+ Z_1(V_+) - V_- Z_1(V_-)}{V_+ - V_-} \right]
\end{aligned}
\tag{C.3}
$$

For trapped particles, there is no contribution to the momentum flux at lowest order in $\epsilon$ because the functional is odd in $\xi$ due to the multiplication by $v_\parallel$ of the linear response. However, when expanding up to first order in $\sqrt{\epsilon}$, there is a net contribution from trapped particles, detailed in (C.4).

$$
\mathcal{J}_{s,tr} = 2\bar{\omega}_b \left[ \left( \frac{R}{L_u} + \frac{u_\parallel}{v_{Ts}} \left( \frac{R}{L_{ns}} - \frac{5}{2} \frac{R}{L_{Ts}} - \frac{\varpi}{n\bar{\omega}_{ds}} \right) \right) \frac{Z_2(z)}{z} + \frac{u_\parallel}{v_{Ts}} \frac{R}{L_{Ts}} \frac{Z_3(z)}{z} \right]
\tag{C.4}
$$

## Appendix D. Fluid model derivation

The fluid limit approximation consists in considering events sufficiently fast decorrelated by collisions such that $\varpi = \omega - n\omega_{E \times B} \gg \bar{\omega}_{di}$ and $\varpi \gg k_\parallel v_{\parallel i}$. This approximation enables the resonance to be developed in power of the small quantities $\frac{\omega_{ds}}{\varpi}$, $\frac{k_\parallel v_\parallel}{\varpi}$ and obtain a polynomial expression in $\varpi$ as detailed in (D.1).

For short wavelengths: $k_\perp \rho_i < 1$, the Pade approximation is performed: $\mathcal{B}_0(k_\perp \rho_i) \approx 1 - \frac{k_\perp^2 \rho_i^2}{2}$. At this spatial scale events are sufficiently slow such that $\omega \ll k_\parallel v_{\parallel e}$. Passing electrons are then considered adiabatic. In contrast, TEM space and time scales being the same as ions modes, trapped electrons are treated by the model. Since $k_r \delta_e < k_r \rho_i < 1$, the Bessel functions on trapped electrons are considered close to unity $\mathcal{B}_0(k_r \delta_e) \approx 1$. For trapped ions, the finite banana width effects are expended in power of $k_r$ too: $\mathcal{B}_0(k_r \delta_i) \approx 1 - \frac{k_r^2 \delta_i^2}{2}$. The resulting expression for the eigenmode is given in (D.1).

$$
\begin{aligned}
&\left[ \frac{n_e}{T_e} \left( \left\langle 1 - \left( 1 - \frac{n\omega_e^*}{\varpi} \right) \left( 1 + \frac{n\omega_{de}}{\varpi} \right) \right\rangle_t + f_p \right) + \right. \\
&\sum_i \frac{n_i Z_i^2}{T_i} \left\langle \left( 1 - \left( 1 - \frac{n\omega_i^*}{\varpi} \right) \left( 1 + \frac{n\omega_{di}}{\varpi} \right) \right) \left( 1 - \frac{k_r^2 \delta_i^2}{4} \right) \right\rangle_t + \\
&\left. \sum_i \frac{n_i Z_i^2}{T_i} \left\langle \left( 1 - \left( 1 - \frac{n\omega_i^*}{\varpi} \right) \left( 1 + \frac{n\omega_{di}}{\varpi} + \frac{k_\parallel v_{\parallel i}}{\varpi} + \frac{k_\parallel^2 v_{\parallel i}^2}{\varpi^2} \right) \right) \left( 1 - \frac{k_\perp^2 \rho_i^2}{2} \right) \right\rangle_p \right] \tilde{\phi} = 0
\end{aligned}
\tag{D.1}
$$

The integration over $k_r$ present in (8) is not performed in (D.1) since $\theta = k_r d$ and $\theta$ is a parallel coordinate label in the ballooning representation. The goal of the model being to capture the radial and parallel variations of the eigenfunction, capturing the dependence on $k_r$ is crucial. This is done through an inverse Fourier transform from $k_r$ to $x$. But first, (D.1) is simplified by using the electroneutrality condition $\sum_i n_i Z_i^2 = n_e$. To simplify (D.1), new quantities are defined: $c_{eff} = \sqrt{\frac{T_e}{m_p}}$ is an effective thermal velocity, $\delta_{eff}^2 = \frac{3}{4}(1 + \frac{f_t}{f_p}\frac{q^2}{4\epsilon})\frac{4m_p T_e}{e^2 B^2}$ represents both finite ion Larmor radius and banana width effects. Finally $\tau = T_i/T_e$. Moreover, considering the low Mach number limit, only the terms linear in $\frac{u_\parallel}{v_{Ts}}$ are kept.

$$
\frac{n_e}{T_e}\left[ f_p \left(1 - \frac{n\omega_{ne}^*}{\varpi} + \left(\frac{2n\omega_d}{\varpi} + \frac{k_\theta^2 \rho_{eff}^2}{2} + \frac{k_r^2 \delta_{eff}^2}{2} - \frac{k_\parallel^2 c_{eff}^2}{2\varpi^2}\right)\left(1 + \frac{n\omega_{pi}^*}{\varpi}\right)\right) - \right.
$$
$$
\left. f_p \left(\frac{n\omega_u^*}{\varpi} + \frac{u_\parallel}{c_{eff}}\left(\frac{Z_{eff}}{\tau} + \frac{n\omega_{ne}^*}{\varpi} - \frac{8n\bar\omega_d}{\varpi}\right)\right)\frac{k_\parallel c_{eff}}{\varpi} + \frac{f_t}{2}\frac{n\bar\omega_d n\omega_{pe}^*}{\varpi^2} \right]\tilde\phi = 0
\tag{D.2}
$$

The passing particle curvature drift reads: $n\omega_d = n\bar\omega_d(\cos(k_r d) + (\hat{s}k_r d - \alpha\sin(k_r d))\sin(k_r d))$ since $\theta = k_r d$. $n\bar\omega_d = n\bar\omega_{de} = -1/\tau n\bar\omega_{di}$. As the ITG turbulence exhibits ballooned modes around $\theta = 0$ [68] (which was used for our ballooning representation simplification [1]), the following linearization is possible: $n\omega_d \to n\bar\omega_d(1 + 1 + (k_r d)^2(\hat{s} - \alpha - 0.5))$ [see 34, App. A]. After this operation, (D.2) is finally polynomial in $k_r$. The inverse Fourier transform in $k_r$ is then performed. The structure of a second order differential equation becomes clear as $k_r$ is transformed into $-i\frac{d}{dx}$.

(D.2) is multiplied by $\varpi^2$ and $\varpi$ is replaced by $\omega - n\omega_{E\times B}$ to make the $x$ dependence of $\varpi$ appear. Indeed, a radial dependence in $\omega_{E\times B}$ is taken into account. The radial electric field is considered smooth enough such that it can be linearized into $E_r \to E_{r0} + E_r' x + O(x^2)$ with $x = r - r_0$ being a small parameter. Therefore, $n\omega_{E\times B} = \frac{k_\theta E_r}{B} \to \frac{k_\theta E_{r0}}{B} + \frac{k_\theta E_r'}{B}x + O(x^2) = n\omega_{E0} + k_\theta\gamma_E x + O(x^2)$. $\omega$ considered below is $\omega - n\omega_{E0}$ since this Doppler shift does not modify the stability of the mode.

$$
\left[\left(\omega\left(\frac{d_{eff}^2}{2}\frac{d^2}{dx^2} - \frac{k_\theta^2\rho_{eff}^2}{2}\right) - 2n\bar\omega_d + \frac{k_\parallel'^2 c_{eff}^2}{2\omega}x^2\right)(\omega - k_\theta\gamma_E x - n\omega_{pi}^*) - \frac{f_t}{f_p}n\omega_{pe}^* n\bar\omega_d \right.
$$
$$
\left. - (\omega - k_\theta\gamma_E x)(\omega - k_\theta\gamma_E x - n\omega_{ne}^*) + k_\parallel' c_{eff}\left(n\omega_u^* + \frac{u_\parallel}{c_{eff}}\left(\frac{Z_{eff}}{\tau}\omega + n\omega_{ne}^* - 8n\bar\omega_d\right)\right)x \right]\tilde\phi = 0
\tag{D.3}
$$

$d_{eff}$ is defined as $d_{eff} = \delta_{eff}^2 + 4\frac{n\bar\omega_d}{\omega}(\hat{s} - \alpha - 0.5)d^2$, containing all terms proportional to $k_r^2$. (D.3) is not linear and there is no general analytic solution of it. But, the ballooning representation used to derive the gyrokinetic dispersion relation (9) assumes a ballooned turbulence around $\theta = 0$. This is not correct if $\gamma_E \gg \omega$. $x$ being small, any term in $k_\perp x$ and $x^3$ or superior are neglected. This results in the following second order linear
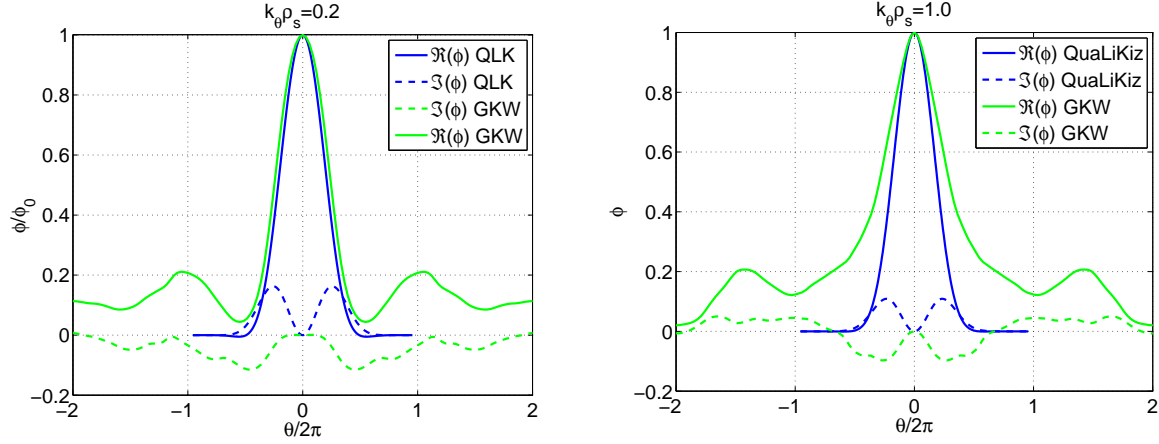
**Figure E1.** Parallel structure of the eigenfunctions showing the increased $\theta$ spreading with $k_\theta\rho_s$ in the case of TEM. $R/L_{Ti} = 0$, other parameters from GA-std test case. $k_\theta\rho_s = 0.2$ left panel. $k_\theta\rho_s = 1.0$ right panel.

differential equation:

$$
\left[ \left( \omega \left( \frac{d_{\text{eff}}^2}{2} \frac{\mathrm{d}^2}{\mathrm{d}x^2} - \frac{k_\theta^2 \rho_{\text{eff}}^2}{2} \right) + \frac{k_\parallel'^2 c_{\text{eff}}^2}{2\omega} x^2 \right) (\omega - n\omega_{pi}^*) - 2n\bar{\omega}_d(\omega - k_\theta\gamma_E) - \omega^2 + 2k_\theta\gamma_E + \right.
$$
$$
\left. (\omega - k_\theta\gamma_E)\, n\omega_{ne}^* - \frac{f_t}{f_p} n\omega_{pe}^* n\bar{\omega}_d + k_\parallel' c_{\text{eff}} \left( n\omega_u^* + \frac{u_\parallel}{c_{\text{eff}}} \left( \frac{Z_{\text{eff}}}{\tau}\omega + n\omega_{ne}^* - 8n\bar{\omega}_d \right) \right) x \right] \tilde{\phi} = 0
$$
$$
(\text{D.4})
$$

## Appendix E. Eigenmodes in strong TEM cases

A GA-std case with $R/L_{Ti} = 0$ keeping $R/L_{Te} = 9$ is studied; in this case TEM are strongly dominant. In Figure E1, QuaLiKiz eigenmodes are compared to GKW for two poloidal wave numbers values: $k_\theta\rho_s = 0.2$ and $k_\theta\rho_s = 1.0$. As foreseen, looking at the real part of the eigenmodes, GKW ones extent over a large domain $|\theta| > \pi$ which is not captured by our fluid model. In contrast, the agreement is satisfactory for $\theta$ inside $[-\pi; \pi]$, which is consistent with the restriction made in QuaLiKiz in the ballooning representation. However, GKW $\tilde{\phi}$ imaginary part flips sign between ITG and TEM whereas QuaLiKiz one remains positive. Finally, inside $[-\pi; \pi]$, the agreement between QuaLiKiz and GKW is better at lower $k_\theta\rho_s$ as expected due to the linearization of the Bessel functions in the fluid model. This is important since $k_\theta\rho_s \approx 0.2$ corresponds to the spatial scales responsible for most of the transport. Overall, in cases where TEM are strongly dominant, it can be foreseen that the growth rates predicted by QuaLiKiz will be underestimated compared to self-consistent gyrokinetic simulations and this underestimation will increase with increasing $k_\theta\rho_s$. Nevertheless, the ion temperature gradients are never zero in experimental cases. Thus realistic eigenfunctions are generally well reproduced by the fluid model used in QuaLiKiz.

## References

[1] Bourdelle C, Garbet X, Hoang G, Ongena J and Budny R 2002 *Nuclear Fusion* **42** 892–902 ISSN 0029-5515

[2] Bourdelle C, Garbet X, Imbeaux F, Casati A, Dubuit N, Guirlet R and Parisot T 2007 *Physics of Plasmas* **14** 112501 ISSN 1070-664X

[3] Casati A, Bourdelle C, Garbet X, Imbeaux F, Candy J, Clairet F, Dif-Pradalier G, Falchetto G, Gerbaud T, Grandgirard V, Guercan O D, Hennequin P, Kinsey J, Ottaviani M, Sabot R, Sarazin Y, Vermare L and Waltz R E 2009 *NUCLEAR FUSION* **49** 085012 ISSN 0029-5515

[4] Tala T, Zastrow K D, Ferreira J, Mantica P, Naulin V, Peeters A G, Tardini G, Brix M, Corrigan G, Giroud C and Strintzi D 2009 *Physical Review Letters* **102**(7) 075001 URL http://link.aps.org/doi/10.1103/PhysRevLett.102.075001

[5] Biglari H, Diamond P and Terry P 1990 *Physics of Fluids B-Plasma Physics* **2** 1–4 ISSN 0899-8221

[6] Ida K, Hidekuma S, Miura Y, Fujita T, Mori M, Hoshino K, Suzuki N and Yamauchi T 1990 *Physical Review Letters* **65** 1364–1367 ISSN 0031-9007

[7] Stambaugh R, Wolfe S, Hawryluk R, Harris J, Biglari H, Prager S, Goldston R, Fonck R, Ohkawa T, Logan B and Oktay E 1990 *Physics of Fluids B-Plasma Physics* **2** 2941–2960 ISSN 0899-8221

[8] Burrell K 1997 *Physics of Plasmas* **4** 1499–1518 ISSN 1070-664X 38th Annual Meeting of the Division-of-Plasma-Physics of the American-Physical-Society, Denver, Co, Nov 11-15, 1996

[9] de Vries P C, Hua M D, McDonald D C, Giroud C, Janvier M, Johnson M F, Tala T, Zastrow K D and Contributors J E 2008 *Nuclear Fusion* **48** 065006 ISSN 0029-5515

[10] Rice J, Lee W, Marmar E, Basse N, Bonoli P, Greenwald M, Hubbard A, Hughes J, Hutchinson I, Ince-Cushman A, Irby J, Lin Y, Mossessian D, Snipes J, Wolfe S, Wukitch S and Zhurovich K 2004 *Physics of Plasmas* **11** 2427–2432 ISSN 1070-664X 45th Annual Meeting of the Division of Plasma Physics of the American-Physical-Society, Albuquerque, Nm, Nov, 2003

[11] Abiteboul J, Ghendrih P, Grandgirard V, Cartier-Michaud T, Dif-Pradalier G, Garbet X, Latu G, Passeron C, Sarazin Y, Strugarek A, Thomine O and Zarzoso D 2013 *Plasma Physics and Controlled Fusion* **55** 074001 URL http://stacks.iop.org/0741-3335/55/i=7/a=074001

[12] Fenzi C, Garbet X, Trier E, Hennequin P, Bourdelle C, Aniel T, Colledani G, Devynck P, Gil C, Guercan O, Manenc L, Schneider M, Segui J L and Team T S 2011 *NUCLEAR FUSION* **51** 103038 ISSN 0029-5515

[13] Groebner R, Burrell K and Seraydarian R 1990 *Physical Review Letters* **64** 3015–3018 ISSN 0031-9007

[14] Scott S, Diamond P, Fonck R, Goldston R, Howell R, Jaehnig K, Schilling G, Synakowski E, Zarnstorff M, Bush C, Fredrickson E, Hill K, Janos A, Mansfield D, Owens D, Park H, Pautasso G, Ramsey A, Schivell J, Tait G, Tang W and Taylor G 1990 *Physical Review Letters* **64** 531–534 ISSN 0031-9007

[15] Honda M, Takizuka T, Fukuyama A, Yoshida M and Ozeki T 2009 *Nuclear Fusion* **49** 035009 ISSN 0029-5515

[16] Eriksson L, Hoang G and Bergeaud V 2001 *Nuclear Fusion* **41** 91–97 ISSN 0029-5515

[17] D'Angelo N 1965 *Physics of Fluids* **8** 1748–1750 URL http://link.aip.org/link/?PFL/8/1748/1

[18] Artun M and Tang W M 1992 *Physics of Fluids B-Plasma Physics* **4** 1102–1114 ISSN 0899-8221

[19] Peeters A and Angioni C 2005 *Physics of Plasmas* **12** 072515 ISSN 1070-664X

[20] Staebler G, Kinsey J and Waltz R 2005 *PHYSICS OF PLASMAS* **12** 102508 ISSN 1070-664X

[21] Kinsey J, Staebler G and Waltz R 2008 *Physics of Plasmas* **15**(5) 055908–1–14 ISSN 1070-664X

[22] Staebler G M, Waltz R E, Candy J and Kinsey J E 2013 *Physical Review Letters* **110** 055003 ISSN 0031-9007

[23] Garbet X and Waltz R 1996 *PHYSICS OF PLASMAS* **3** 1898–1907 ISSN 1070-664X 37th Annual Meeting of the Division-of-Plasma-Physics of the American-Physical-Society, LOUISVILLE, KY, NOV 06-10, 1995

[24] Waltz R, Dewar R and Garbet X 1998 *Physics of Plasmas* **5** 1784–1792 ISSN 1070-664X 39th Annual Meeting of the Division-of-Plasma-Physics of the American-Physical-Society, Pittsburgh, Pennsylvania, Nov 17-21, 1997

[25] Angioni C, McDermott R M, Fable E, Fischer R, Puetterich T, Ryter F, Tardini G and Team A U 2011 *NUCLEAR FUSION* **51** 023006 ISSN 0029-5515

[26] Camenen Y, Peeters A G, Angioni C, Casson F J, Hornsby W A, Snodin A P and Strintzi D 2009 *PHYSICS OF PLASMAS* **16** 012503 ISSN 1070-664X

[27] Barnes M, Parra F I, Highcock E G, Schekochihin A A, Cowley S C and Roach C M 2011 *Physical Review Letters* **106**(17) 175004 URL http://link.aps.org/doi/10.1103/PhysRevLett.106.175004

[28] Highcock E G, Barnes M, Schekochihin A A, Parra F I, Roach C M and Cowley S C 2010 *PHYSICAL REVIEW LETTERS* **105** 215003 ISSN 0031-9007

[29] Kinsey J, Waltz R and Candy J 2005 *Physics of Plasmas* **12** 062302 ISSN 1070-664X

[30] Peeters A G, Angioni C, Bortolon A, Camenen Y, Casson F J, Duval B, Fiederspiel L, Hornsby W A, Idomura Y, Hein T, Kluy N, Mantica P, Parra F I, Snodin A P, Szepesi G, Strintzi D, Tala T, Tardini G, de Vries P and Weiland J 2011 *Nuclear Fusion* **51** 094027 ISSN 0029-5515

[31] Roach C M, Abel I G, Akers R J, Arter W, Barnes M, Camenen Y, Casson F J, Colyer G, Connor J W, Cowley S C, Dickinson D, Dorland W, Field A R, Guttenfelder W, Hammett G W, Hastie R J, Highcock E, Loureiro N F, Peeters A G, Reshko M, Saarelma S, Schekochihin A A, Valovic M and Wilson H R 2009 *Plasma Physics And Controlled Fusion* **51** 124020 ISSN 0741-3335 36th European-Physical-Society Conference on Plasma Physics, Natl Palace Culture, Sofia, Bulgaria, Jun 29-Jul 03, 2009

[32] Waltz R E, Staebler G M, Candy J and Hinton F L 2007 *Physics of Plasmas* **14** 122507 ISSN 1070-664X

[33] Strugarek A, Sarazin Y, Zarzoso D, Abiteboul J, Brun A S, Cartier-Michaud T, Dif-Pradalier G, Garbet X, Ghendrih P, Grandgirard V, Latu G, Passeron C and Thomine O 2013 *Plasma Physics and Controlled Fusion* **55** 074013 URL `http://stacks.iop.org/0741-3335/55/i=7/a=074013`

[34] Romanelli M, Regnoli G and Bourdelle C 2007 *Physics of Plasmas* **14** 082305 ISSN 1070-664X

[35] Artaud J F, Basiuk V, Imbeaux F, Schneider M, Garcia J, Giruzzi G, Huynh P, Aniel T, Albajar F, Ane J M, Becoulet A, Bourdelle C, Casati A, Colas L, Decker J, Dumont R, Eriksson L G, Garbet X, Guirlet R, Hertout P, Hoang G T, Houlberg W, Huysmans G, Joffrin E, Kim S H, Koechl F, Lister J, Litaudon X, Maget P, Masset R, Pegourie B, Peysson Y, Thomas P, Tsitroneand E and Turco F 2010 *NUCLEAR FUSION* **50** 043001 ISSN 0029-5515

[36] Baiocchi B, Garcia J, Beurkens M, Bourdelle C, Crisanti F, Giroud C, Hobirk J, Imbeaux F, Nunes I, group E I I S M and contributors J E 2013 *40th EPS Conference on Plasma Physics* vol P2 (European Physical Society) p 165

[37] Waltz R E, Staebler G M and Solomon W M 2011 *Physics of Plasmas* **18** 042504 ISSN 1070-664X

[38] Camenen Y, Idomura Y, Jolliet S and Peeters A G 2011 *Nuclear Fusion* **51** 073039 ISSN 0029-5515

[39] Gürcan O D, Diamond P H, Hennequin P, McDevitt C J, Garbet X and Bourdelle C 2010 *Physics of Plasmas* **17** 112309 ISSN 1070-664X

[40] Peeters A G, Camenen Y, Casson F J, Hornsby W A, Snodin A P, Strintzi D and Szepesi G 2009 *Computer Physics Communications* **180** 2650–2672 ISSN 0010-4655

[41] Tala T, Crombé K, de Vries P, Ferreira J, Mantica P, Peeters A, Andrew Y, Budny R, Corrigan G, Eriksson A, Garbet X, Giroud C, Hua M D, Nordman H, Naulin V, Nave M, Parail V, Rantamäki K, Scott B D, Strand P, Tardini G, Thyagaraja A, Weiland J, Zastrow K D and Contributors J E 2007 *Plasma Physics and Controlled Fusion* **49** B291 URL `http://stacks.iop.org/0741-3335/49/i=12B/a=S27`

[42] Garbet X, Laurent L, Mourgues F, Roubin J and Samain A 1990 *Journal Of Computational Physics* **87** 249–269 ISSN 0021-9991

[43] Rutherford P and Frieman E 1968 *Physics of Fluids* **11** 569–& ISSN 1070-6631

[44] Taylor J and Hastie R 1968 *Plasma Physics* **10** 479–&

[45] Antonsen T M and Lane B 1980 *Physics of Fluids* **23** 1205–1214 ISSN 1070-6631

[46] Catto P, Tang W and Baldwin D 1981 *Plasma Physics and Controlled Fusion* **23** 639–650 ISSN 0741-3335

[47] Littlejohn R 1981 *Physics of Fluids* **24** 1730–1749 ISSN 1070-6631

[48] Hahm T 1988 *Physics Of Fluids* **31** 2670–2673 ISSN 1070-6631

[49] Brizard A 1989 *Physics of Fluids B-Plasma Physics* **1** 1381–1384 ISSN 0899-8221

[50] Brizard A J and Hahm T S 2007 *Reviews of Modern Physics* **79** 421–468 ISSN 0034-6861

[51] Lapillonne X, Brunner S, Dannert T, Jolliet S, Marinoni A, Villard L, Goerler T, Jenko F and Merz F 2009 *Physics of Plasmas* **16** 032308 ISSN 1070-664X

[52] Casson F J, Peeters A G, Angioni C, Camenen Y, Hornsby W A, Snodin A P and Szepesi G 2010 *Physics of Plasmas* **17** 102305 ISSN 1070-664X

[53] Bourdelle C, Dorland W, Garbet X, Hammett G, Kotschenreuther M, Rewoldt G and Synakowski E 2003 *PHYSICS OF PLASMAS* **10** 2881–2887 ISSN 1070-664X

[54] Connor J, Hastie R and Taylor J 1978 *Physical Review Letters* **40** 396–399 ISSN 0031-9007

[55] Pegoraro F and Schep T 1981 *Physics of Fluids* **24** 478–497 ISSN 1070-6631

[56] Dewar R and Glasser A 1983 *Physics of Fluids* **26** 3038–3052 ISSN 1070-6631

[57] Candy J, Waltz R and Rosenbluth M 2004 *PHYSICS OF PLASMAS* **11** 1879–1890 ISSN 1070-664X

[58] Citrin J, Bourdelle C, Cottier P, Escande D F, Guercan O D, Hatch D R, Hogeweij G M D, Jenko F and Pueschel M J 2012 *Physics of Plasmas* **19** 062305 ISSN 1070-664X

[59] COOPER W 1988 *PLASMA PHYSICS AND CONTROLLED FUSION* **30** 1805–1812 ISSN 0741-3335

[60] MILLER R and WALTZ R 1994 *PHYSICS OF PLASMAS* **1** 2835–2842 ISSN 1070-664X

[61] Mattor N and Diamond P 1988 *Physics of Fluids* **31** 1180–1189 ISSN 1070-6631

[62] Dong J and Horton W 1993 *Physics of Fluids B-Plasma Physics* **5** 1581–1592 ISSN 0899-8221

[63] Garbet X, Sarazin Y, Ghendrih P, Benkadda S, Beyer P, Figarella C and Voitsekhovitch I 2002 *Physics of Plasmas* **9** 3893–3905 ISSN 1070-664X

[64] Gurcan O D, Diamond P H, Hahm T S and Singh R 2007 *PHYSICS OF PLASMAS* **14** 042306 ISSN 1070-664X

[65] Hahm T S, Diamond P H, Gurcan O D and Rewoldt G 2007 *PHYSICS OF PLASMAS* **14** 072302 ISSN 1070-664X

[66] Waltz R E, Staebler G M, Dorland W, Hammett G W, Kotschenreuther M and Konings J A 1997 *Physics of Plasmas* **4** 2482–2496 ISSN 1070-664X

[67] HAMADA S 1959 *PROGRESS OF THEORETICAL PHYSICS* **22** 145–146 ISSN 0033-068X

[68] Brunner S, Fivaz M, Tran T and Vaclavik J 1998 *PHYSICS OF PLASMAS* **5** 3929–3949 ISSN 1070-664X

[69] Casson F J, Peeters A G, Angioni C, Camenen Y, Hornsby W A, Snodin A P and Szepesi G 2012 *PHYSICS OF PLASMAS* **19** 099902 ISSN 1070-664X

[70] Waltz R, Kerbel G and Milovich J 1994 *Physics of Plasmas* **1** 2229–2244 ISSN 1070-664X

[71] Hahm T and Burrell K 1995 *Physics of Plasmas* **2** 1648–1651 ISSN 1070-664X

[72] Citrin J, Bourdelle C, Haverkort J W, Hogeweij G M D, Jenko F, Mantica P, Pueschel M J, Told D and contributors J E 2013 *Nuclear Fusion* **53**

[73] Casson F J, Peeters A G, Camenen Y, Hornsby W A, Snodin A P, Strintzi D and Szepesi G 2009 *Physics Of Plasmas* **16** 092303 ISSN 1070-664X

[74] Angioni C, Peeters A, Garbet X, Manini A, Ryter F and Team A U 2004 *NUCLEAR FUSION* **44** 827–845 ISSN 0029-5515

[75] Angioni C, Camenen Y, Casson F J, Fable E, McDermott R M, Peeters A G and Rice J E 2012 *NUCLEAR FUSION* **52** 114003 ISSN 0029-5515 13th International Workshop on H-Mode Physics and Transport Barriers, Lady Margaret Hall Coll, Oxford, ENGLAND, OCT, 2011

[76] Dannert T and Jenko F 2005 *PHYSICS OF PLASMAS* **12** 072309 ISSN 1070-664X

[77] Kinsey J, Staebler G and Waltz R 2005 *PHYSICS OF PLASMAS* **12** 052503 ISSN 1070-664X

[78] Merz F and Jenko F 2010 *NUCLEAR FUSION* **50** 054005 ISSN 0029-5515 4th IAEA Technical Meeting on the Theory of Plasma Instabilities, Kyoto, JAPAN, MAY 18-20, 2009

[79] Staebler G M, Kinsey J E and Waltz R E 2007 *PHYSICS OF PLASMAS* **14** 055909 ISSN 1070-664X 48th Annual Meeting of the Division of Plasma Physics of the APS, Philadelphia, PA, JAN 30-NOV 03, 2006

[80] Waltz R E, Casati A and Staebler G M 2009 *PHYSICS OF PLASMAS* **16** 072303 ISSN 1070-664X

[81] Abiteboul J, Garbet X, Grandgirard V, Allfrey S J, Ghendrih P, Latu G, Sarazin Y and Strugarek A 2011 *PHYSICS OF PLASMAS* **18** 082503 ISSN 1070-664X

[82] McKee G, Petty C, Waltz R, Fenzi C, Fonck R, Kinsey J, Luce T, Burrell K, Baker D, Doyle E, Garbet X, Moyer R, Rettig C, Rhodes T, Ross D, Staebler G, Sydora R and Wade M 2001 *NUCLEAR FUSION* **41** 1235–1242 ISSN 0029-5515

[83] Jenko F and Dorland W 2002 *PHYSICAL REVIEW LETTERS* **89** 225001 ISSN 0031-9007

[84] Connor J W 2006 *PLASMA PHYSICS REPORTS* **32** 539–548 ISSN 1063-780X